PHYSICAL REVIEW D **72,** 064014 (2005)

Reconstructing the Universe

J. Ambjørn,[1,3,*] J. Jurkiewicz,[2,†] and R. Loll[3,‡]

[1]*The Niels Bohr Institute, Copenhagen University, Blegdamsvej 17, DK-2100 Copenhagen Ø, Denmark*

[2]*Mark Kac Complex Systems Research Centre, Marian Smoluchowski Institute of Physics, Jagellonian University, Reymonta 4, PL 30-059 Krakow, Poland*

[3] *Institute for Theoretical Physics, Utrecht University, Leuvenlaan 4, NL-3584 CE Utrecht, The Netherlands*

(Received 24 June 2005; published 22 September 2005)

We provide detailed evidence for the claim that nonperturbative quantum gravity, defined through state sums of causal triangulated geometries, possesses a large-scale limit in which the dimension of spacetime is four and the dynamics of the volume of the universe behaves semiclassically. This is a first step in reconstructing the universe from a dynamical principle at the Planck scale, and at the same time provides a nontrivial consistency check of the method of causal dynamical triangulations. A closer look at the quantum geometry reveals a number of highly nonclassical aspects, including a dynamical reduction of spacetime to two dimensions on short scales and a fractal structure of slices of constant time.

DOI: 10.1103/PhysRevD.72.064014 PACS numbers: 04.60.Gw, 04.60.Nc

I. INTRODUCTION

Nonperturbative quantum gravity can be defined as the quest for uncovering the true dynamical degrees of freedom of spacetime geometry at the very shortest scales. Because of the enormous quantum fluctuations predicted by the uncertainty relations, geometry near the Planck scale will be extremely rugged and nonclassical. Although different approaches to quantizing gravity do not agree on the precise nature of these fundamental excitations, or on how they can be determined, most of the popular formulations[1] agree that they are neither the smooth metrics $g_{\mu\nu}(x)$ (or equivalent classical field variables) of general relativity nor straightforward quantum analogues thereof. In such scenarios, one expects the metric to re-emerge as an appropriate description of spacetime geometry only at larger scales.

Giving up the spacetime metric at the Planck scale does not mean discarding geometry altogether, since geometric properties such as the presence of a distance function pertain to much more general structures than differential manifolds with smooth metric assignments. One could hope that quantum gravity, when formulated in terms of the conjectured new microscopic degrees of freedom, was better behaved in the ultraviolet regime than standard perturbative approaches based on the spacetime metric. At the same time, it becomes a nontrivial test for such nonperturbative theories of quantum gravity whether they can reproduce the correct classical limit at sufficiently large scales. However, using this as a consistency check to discriminate between good and bad candidate theories is in practice complicated by the fact that *some* explicit results about the quantum dynamics of the proposed quantum gravity theory must be known. For example, this is not yet the case in loop quantum gravity [4–6] or in four-dimensional spin foam models for gravity [7].

In the method of *Causal Dynamical Triangulations* one tries to construct a theory of quantum gravity as a suitable continuum limit of a superposition of spacetime geometries [8–10]. In close analogy with Feynman's famous path integral for the nonrelativistic particle, one works with an intermediate regularization in which the geometries are piecewise flat[2]. The primary object of interest in this approach is the propagator between two boundary configurations (in the form of an initial and final spatial geometry), which contains the complete dynamical information about the quantum theory. Because of the calculational complexity of the full, nonperturbative sum over geometries (the ''path integral''), an analytical evaluation is at this stage out of reach. Nevertheless, powerful computational tools, developed in Euclidean quantum gravity [11–17] and other theories of random geometry (see [18] for a review), can be brought to bear on the problem.

This paper describes in detail how Monte Carlo simulations have been used to extract information about the quantum theory, and, in particular, the geometry of the quantum ground state[3] dynamically generated by super-

*Email address: ambjorn@nbi.dk

†Email address: jurkiewicz@th.if.uj.edu.pl

‡Email address: r.loll@phys.uu.nl

[1]An exception are renormalization group approaches which look for nontrivial ultraviolet fixed points in a metric formulation [1–3].

[2]These are the analogues of the piecewise straight paths of Feynman's approach. However, note that the geometric configurations of the quantum-gravitational path integral are *not* imbedded into a higher-dimensional space, and therefore their geometric properties such as piecewise flatness are intrinsic, unlike in the case of the particle paths.

[3]Here and in the following, by ''ground state'' we will always mean the state selected by Monte Carlo simulations, performed under the constraint that the volume of spacetime is (approximately) kept fixed, a constraint we have to impose for simulation-technical reasons.

posing causal triangulations. It follows the announcement of several key results in this approach to quantum gravity, first, a ''quantum derivation'' of the fact that spacetime is macroscopically four-dimensional [19], second, a demonstration that the large-scale dynamics of the spatial volume of the universe (the so-called ''scale factor'') observed in causal dynamical triangulations can be described by an effective action closely related to standard quantum cosmology [20], and third, the discovery that in the limit of short distances, spacetime becomes effectively two-dimensional, indicating the presence of a dynamically generated ultraviolet cutoff [21]. They do not provide conclusive proof that our construction from first principles *does* lead to a viable theory of quantum gravity, but go some way in establishing the existence of a physically meaningful classical limit. In addition, our detailed geometric analysis throws some light on the highly nonclassical microscopic properties of the spacetimes dominating the gravitational path integral, which after all are higher-dimensional analogues of the nowhere-differentiable paths that provide the support of Feynman's path integral.

Our presentation will proceed as follows. After recollecting some basic properties of the geometric set-up of the regularized path integral over causal triangulations in Sec. II, we explain in Sec. III how the path integral is implemented numerically. The statistical model underlying our construction possesses three phases, which are distinguished by the geometric nature of their ground states, as described in Sec. IV. From this point on, we concentrate on the phase which yields a ground state which is extended in time and space. In Sec. V we provide the detailed numerical evidence for why this state is four-dimensional at large scales and why its shape can be described by a minisuperspace action. We then embark on a detailed investigation of substructures of the spacetime universe, namely, spatial slices (of fixed integer time τ) in Sec. VI and in Sec. VII ''thick spatial slices'', which are geometries of finite time extension $\Delta\tau = 1$. We measure both their Hausdorff and spectral dimensions, the latter from a discrete diffusion process. Interestingly, the geometry of the ''thin'' spatial slices shares some characteristics with a class of branched polymers which has already appeared in areas as diverse as noncritical string theory, econophysics and network theory. A summary of our results and an outlook are presented in Sec. VIII.

II. GEOMETRIC SET-UP AND SIMPLICIAL ACTION

We briefly remind the reader of the structure of the spacetime geometries which contribute to the regularized path integral [10]. The fundamental building blocks are two types of four-simplices ''cut out of'' four-dimensional flat Minkowski space. A flat four-simplex of type (4,1) has six spacelike edges of length-squared $l^2_{\text{space}} = a^2$ and four timelike edges of length-squared $l^2_{\text{time}} = -\alpha a^2$. Similarly, a flat four-simplex of type (3,2) has four spacelike edges of length-squared $l^2_{\text{space}} = a^2$ and six timelike ones of length-squared $l^2_{\text{time}} = -\alpha a^2$. Each spacetime has a well-defined global foliation by a ''proper time'' τ.[4] Fig. 1 illustrates how the simplicial building blocks are situated between consecutive spatial slices of constant integer τ. The (4,1)-simplex consists of a spatial tetrahedron at time τ whose four vertices are connected by four timelike edges to the single vertex at time $\tau + 1$. Similarly, the (3,2)-simplex consists of a spatial triangle at time τ whose vertices are connected to the two vertices at $\tau + 1$ which form the end points of the fourth spatial edge of the simplex.

The way in which these building blocks, together with their counterparts with inversed time orientation, can form a spacetime slice of height $\Delta\tau = 1$ is by gluing them pairwise along a shared timelike boundary tetrahedron. In order to get a spacetime of time duration $\tau = t$, one glues together t such slices in succession, which is of course only possible whenever their spatial boundary geometries at integer-τ match pairwise. We require the gluings to be such that the resulting discretized spacetime is a simplicial manifold. The spacetime topology is fixed to $[0, 1] \times {}^{(3)}\Sigma$, where for our investigations we have chosen as constant-τ surfaces the three-spheres ${}^{(3)}\Sigma = S^3$. For convenience in the computer simulations, we also sometimes identify time periodically, leading to a spacetime topology $S^1 \times S^3$.

From the edge-length assignments one can compute volumes and interior angles of the simplices which are needed because they appear in the Regge form of the Einstein action, from which the weight of each triangulated spacetime T in the sum over geometries will be computed (see [10] for calculational details). The gravitational action becomes then a simple function of a number of positive integers, which count the overall numbers of simplices or subsimplices of a certain type. For completeness, we give the explicit form of the action after analytic continuation to the Euclidean sector, as a function of the number N_0 of vertices (zero-simplices), and the numbers $N_4^{(3,2)}$ and $N_4^{(4,1)}$ of four-simplices of types (3,2) and (4,1) of either time orientation,

[4]We choose the name ''proper time'' because the *a priori* integer-valued variable τ can be extended continuously to the entire space-time [22]. Within each simplex one can choose a coordinate system whose time variable coincides with τ and also with the proper time of a freely falling observer in the simplex. Note that our setting here is that of piecewise flat and not of smooth geometries.

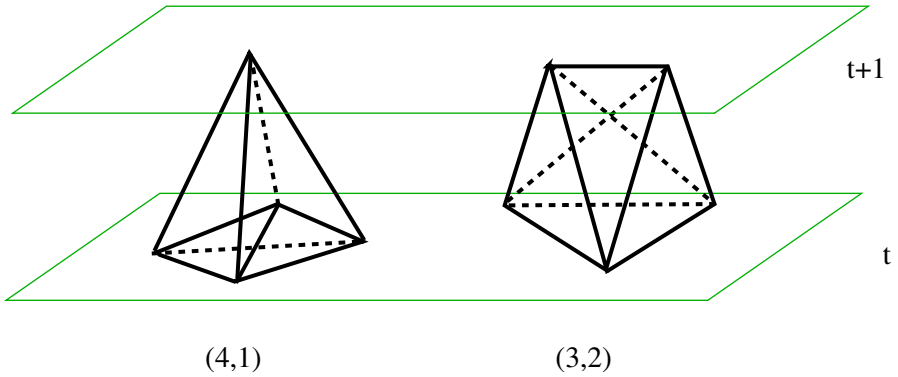

FIG. 1 (color online). The two fundamental building blocks of causal dynamically triangulated gravity. The flat four-simplex of type (4,1) on the left has four of its vertices at time τ and one at time $\tau + 1$, and analogously for the (3,2)-simplex on the right. The "gap" between two consecutive spatial slices of constant integer time is filled by copies of these simplicial building blocks and their time-reversed counterparts, the (1,4)- and the (2,3)-simplices.

$$S_E = -k^{(b)}\pi\sqrt{4\tilde{\alpha}-1}(N_0-\chi) + N_4^{(4,1)}\Big(k^{(b)}\sqrt{4\tilde{\alpha}-1}\Big(-\frac{\pi}{2} - \frac{\sqrt{3}}{\sqrt{4\tilde{\alpha}-1}}\arcsin\frac{1}{2\sqrt{2}\sqrt{3\tilde{\alpha}-1}} + \frac{3}{2}\arccos\frac{2\tilde{\alpha}-1}{6\tilde{\alpha}-2}\Big) + \lambda^{(b)}\frac{\sqrt{8\tilde{\alpha}-3}}{96}\Big) + N_4^{(3,2)}\Big(k^{(b)}\sqrt{4\tilde{\alpha}-1}\Big(-\pi + \frac{\sqrt{3}}{4\sqrt{4\tilde{\alpha}-1}}\arccos\frac{6\tilde{\alpha}-5}{6\tilde{\alpha}-2} + \frac{3}{4}\arccos\frac{4\tilde{\alpha}-3}{8\tilde{\alpha}-4} + \frac{3}{2}\arccos\frac{1}{2\sqrt{2}\sqrt{2\tilde{\alpha}-1}\sqrt{3\tilde{\alpha}-1}}\Big) + \lambda^{(b)}\frac{\sqrt{12\tilde{\alpha}-7}}{96}\Big). \quad (1)$$

In this expression, χ is the Euler characteristic of the piecewise flat four-manifold and $\tilde{\alpha} \equiv -\alpha$ denotes the positive ratio between the two types of squared edge lengths after the Euclideanization. In order to satisfy the triangle inequalities, we need $\tilde{\alpha} > 7/12$ [10]. For simplicity, we have assumed that the manifold is compact without boundaries. In the presence of boundaries, appropriate boundary terms must be added to the action.

For the simulations, a convenient alternative parametrization of the action is given by

$$S_E = -(\kappa_0 + 6\Delta)N_0 + \kappa_4(N_4^{(4,1)} + N_4^{(3,2)}) + \Delta(2N_4^{(4,1)} + N_4^{(3,2)}), \quad (2)$$

where the functional dependence of the κ_i and Δ on the bare inverse Newton constant $k^{(b)}$, the bare cosmological constant $\lambda^{(b)}$ and $\tilde{\alpha}$ can be computed from (1). We have dropped the constant term proportional to χ, because it will be irrelevant for the quantum dynamics. Note that $\Delta = 0$ corresponds to $\tilde{\alpha} = 1$, and Δ is therefore a measure of the asymmetry between the lengths of the spatial and timelike edges of the simplicial geometry. As we shall see, the physically interesting region of the phase diagram of four-dimensional causal dynamical triangulations has positive Δ, which translates into values of $\tilde{\alpha}$ smaller than 1.

III. NUMERICAL IMPLEMENTATION

We have investigated the infinite-volume limit of the ensemble of causal triangulated four-dimensional geometries with the help of Monte Carlo simulations at finite four-volumes $N_4 = N_4^{(4,1)} + N_4^{(3,2)}$ of up to 362.000 four-simplices. A simplicial geometry is stored in the computer as a set of lists, where the lists consist of dynamic sequences of labels for simplices of dimension n, $0 \le n \le 4$, together with their position and orientation with respect to the time direction. Additional list data include information about nearest neighbors, i.e. how the triangulation "hangs together", and other discrete data (for example, how many four-simplices meet at a given edge) which help improve the acceptance rate of Monte Carlo moves.

The simulation is set up to generate a random walk in the ensemble of causal geometries of a fixed time extension t. The local updating algorithm consists of a set of moves that change the geometry of the simplicial manifold locally, without altering its topological properties. These can be understood as a Lorentzian variant of (a simplified version of) the so-called Alexander moves [23–25], in the sense that they are compatible with the discrete time slicing of our causal geometries. For example, the subdivision of a four-simplex into five four-simplices by placing a new vertex at its center is not allowed, because vertices can only be located at integer times τ. Details of the local moves can be found in [10]. As usual, each suggested local change of triangulation is accepted or rejected according to

certain probabilities depending on the change in the action and the local geometry. (Note that a move will always be rejected if the resulting triangulation violates the simplicial manifold property.) The moves are called in random order, with probabilities chosen in such a way as to ensure that the numbers of actually performed moves of each type are approximately equal. We attained a rather high average acceptance rate of about 12.5%, which was made possible by keeping track of subsimplex structures relevant for the performance of certain moves, as mentioned earlier. The attempted moves were performed in units of 10^6 (one "sweep"), with the time for one sweep approximately independent of the system volume in the region $\kappa_0 \approx 2.2$ and $\Delta \approx 0.4 \ldots 0.6$ where most of our measurements were taken.

In order to obtain an efficient sampling of geometries of large four-volume (the larger the four-volume, the better the computer-generated geometries describe the continuum limit), we have performed the simulations at (approximately) constant four-volume. This means that instead of the standard gravitational path integral (after Euclideanization)

$$Z_E(\lambda, G) = \int \mathcal{D}[g] e^{-S_E[g]}, \qquad S_E[g] = -\frac{1}{G} \int d^4x \sqrt{|\det g|}(R - 2\lambda) \tag{3}$$

we simulate a discretized version of the path integral at fixed four-volume V_4,

$$\tilde{Z}_E(V_4, G) = \int \mathcal{D}[g] e^{-\tilde{S}_E[g]} \delta\Big(\int d^4x \sqrt{\det g} - V_4\Big), \qquad \tilde{S}_E[g] = -\frac{1}{G} \int d^4x \sqrt{\det g} R, \tag{4}$$

which is related to (3) by a Laplace transformation,

$$Z_E(\lambda, G) = \int_0^\infty dV_4 e^{-(2/G)\lambda V_4} \tilde{Z}_E(V_4, G). \tag{5}$$

However, the local moves do not in general preserve the numbers $N_4^{(4,1)}$ and $N_4^{(3,2)}$ of four-simplices, or indeed their sum. We deal with this in a standard way which was developed for dynamically triangulated models in dimensions three and four [11,26] to ensure that the system volume is peaked at a prescribed value, with a well-defined range of fluctuations. Adapting it to the current situation of causal triangulations with nonvanishing asymmetry Δ, we implement an approximate four-volume constraint by adding a term

$$\delta S = \epsilon |N_4^{(4,1)} - \tilde{N}_4|, \tag{6}$$

to the Euclidean action, with typical values of ϵ lying in the range of 0.01 to 0.02, except during thermalization where we set $\epsilon = 0.05$. The reason for fixing $N_4^{(4,1)}$ instead of $N_4 = N_4^{(4,1)} + N_4^{(3,2)}$ in Eq. (6) is mere technical convenience. We have checked in the phase-space region relevant to four-dimensional quantum gravity (phase C, see below) that for $N_4^{(4,1)}$ fixed according to (6), the number $N_4^{(3,2)}$ of four-simplices of type (3,2) is likewise very sharply peaked, see Fig. 2. The "four-volumes" $\tilde{N}_4$ and the corresponding "true" discrete four-volumes N_4 used in the simulations are listed in Table I. In order to stabilize the total volume after thermalization, κ_4 has to be fine-tuned to its pseudocritical value (which depends weakly on the volume) with accuracy smaller than ϵ, in practice to about 0.2ϵ. The measurements reported in this paper were taken at $\tilde{N}_4 = 10, 20, 40, 80$ and 160 k, and the runs were performed on individual PCs or a PC farm for the smaller systems and a cluster of work stations for the larger systems.

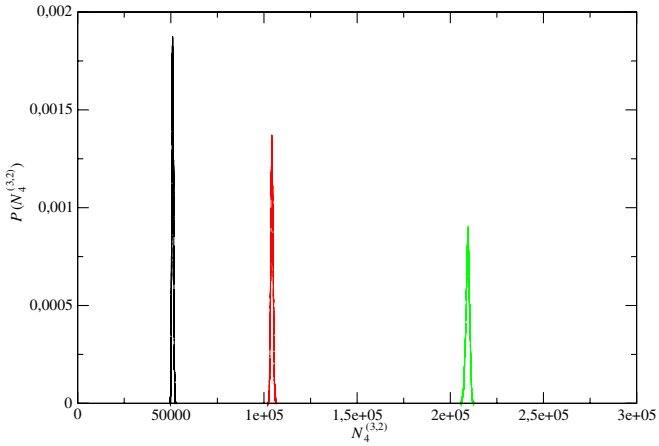

FIG. 2 (color online). Unnormalized distribution of the number $N_4^{(3,2)}$ of four-dimensional simplices of type (3,2), at fixed numbers of four-simplices of type (4,1), for $N_4^{(4,1)} = 40, 80$ and 160 k (left to right) at $\kappa_0 = 2.2$ and $\Delta = 0.6$.

Before measurements can be performed, one needs a well thermalized configuration of a given volume. In order to double-check the quality of the thermalization, we used two different methods to produce starting configurations for the measurement runs. In the first method, we evolved from an initial minimal four-dimensional triangulation of prescribed topology and of a given time extension t, obtained by repeated gluing of a particular triangulated space-time slice of $\Delta\tau = 1$ and topology $[0, 1] \times S^3$, which consists of 30 four-simplices. The spatial in- and

TABLE I. Translation table between the two types of discrete four-volume, $\tilde{N}_4$ and N_4, at which the numerical simulations reported in this article were performed, in units of 1000 building blocks (phase C only).

"four-volume" $\tilde{N}_4 = N_4^{(4,1)}$	10	20	40	80	160
actual four-volume $N_4 = N_4^{(4,1)} + N_4^{(3,2)}$	22.25	45.5	91	181	362

out-geometries of the slice are minimal spheres S^3, made of five tetrahedra. The two types of spatial boundary conditions used are (i) periodic identification of the geometries at initial and final integer times, and (ii) free boundary conditions, where all vertices contained in the initial slice at time τ_0 are connected by timelike edges to a single vertex at time $\tau_0 - 1$, and similarly for the vertices contained in the final spatial slice. From this initial configuration, the geometry evolves to its target volume $\tilde{N}_4$ as specified through δS. During the evolution the volume-volume correlator (see Eq. (7) below) changes from a very broad distribution to the stable narrow shape seen in Fig. 7. The number of sweeps to reach the thermalized configuration changes linearly with $\tilde{N}_4$ and ranged from 10^5 to 10^8 sweeps for the largest volumes, the latter of which took several weeks on a work station.

In the second method, we started instead from a thermalized configuration of smaller volume, which we let evolve towards the target volume. In this case the final volume-volume distribution is reached from a narrower distribution, namely, that of the smaller volume. During thermalization, this width grows very slowly. The timing of the entire process is similar to that of the first method.

IV. PHASE STRUCTURE OF THE MODEL

Like always in dynamically triangulated models, the bare cosmological constant $\lambda^{(b)}$ (equivalently, κ_4) is tuned to its (pseudo-)critical value in the simulations, tantamount to approaching the infinite-volume limit. Depending on the values of the two remaining parameters κ_0 and Δ in the discretized action (2), we have identified three different phases, A, B and C, mutually separated by lines of first-order transitions. We have not yet measured their location in detail; Fig. 3 is a qualitative sketch of the phase diagram. We describe each of the three phases in turn:

(a) This phase prevails for sufficiently large κ_0 (recall κ_0 is proportional to the bare inverse Newton's constant $k^{(b)}$). When plotting the volume of the spatial slices $\tau = \text{const}$ as a function of τ, we observe an irregular sequence of maxima and minima, where the minimal size is of the order of the cutoff, and the sizes of the maxima vary, see Fig. 4. The time intervals during which the spacetime has a macroscopic spatial extension are small and of the order of $\Delta\tau = 3$.

(b) This phase occurs for sufficiently small κ_0 and for small asymmetry Δ, including $\Delta = 0$. In it, spacetime undergoes a "spontaneous dimensional reduction" in the sense that all four-simplices are concentrated in a slice of minimal time extension $\Delta\tau = 2$, and the three-volume $N_3(\tau)$ remains close to its kinematic minimum everywhere else (Fig. 5). We believe that these two phases can be understood essentially from the dynamics of the (Euclidean) geometries of the slices of constant τ alone. The spatial slices in phase A are presumably realizations of branched polymers which dominate the path integral of three-dimensional Euclidean quantum gravity for large κ_0, whereas the extended part of

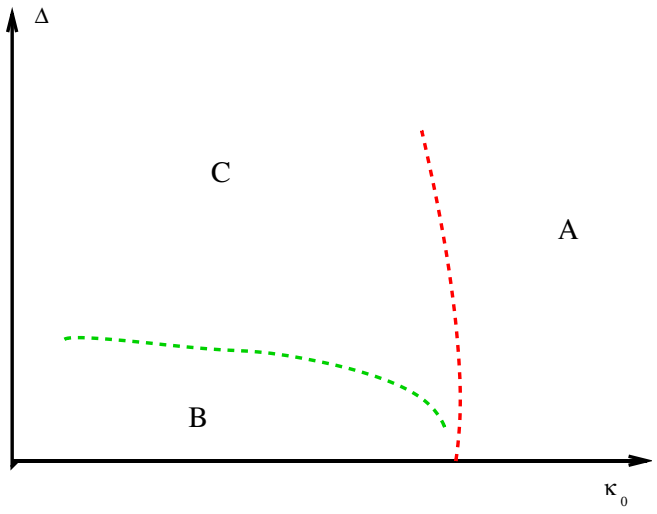

FIG. 3 (color online). A qualitative sketch of the phase diagram of four-dimensional causal dynamical triangulations as function of the gravitational coupling κ_0 and the asymmetry parameter Δ.

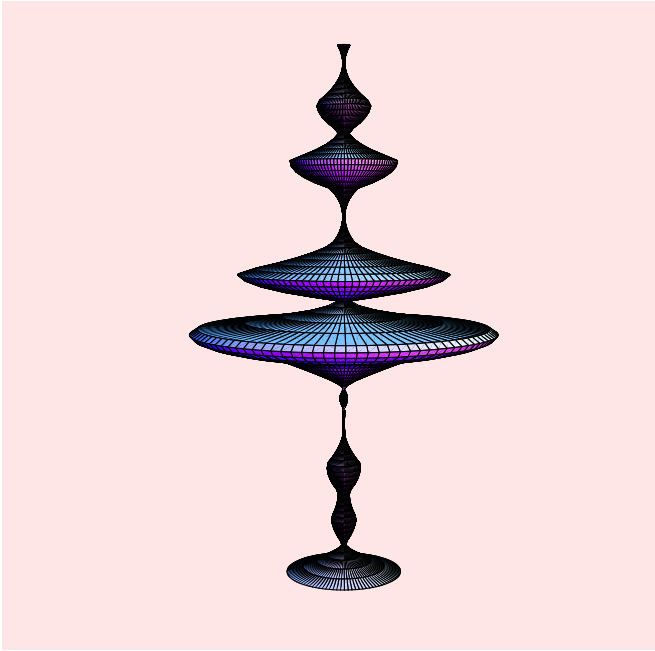

FIG. 4 (color online). Monte Carlo snapshot of a typical universe in phase A ($\kappa_0 = 5.0$, $\Delta = 0$), of discrete volume $N_4 = 45.5$ k and total time extent (vertical direction) $t = 20$. In this and the following two figures, the circumference at integer proper time τ is chosen proportional to the spatial three-volume $V_3(\tau)$. The surface represents an interpolation between adjacent spatial volumes, without capturing the actual 4d connectivity between neighboring spatial slices.

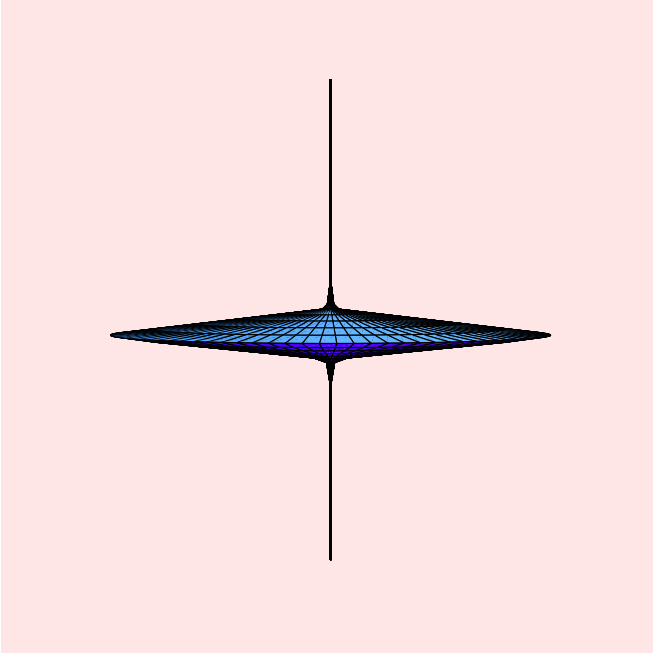

FIG. 5 (color online). Monte Carlo snapshot of a typical universe in phase B ($\kappa_0 = 1.6$), of discrete volume $N_4 = 22.25$ k and total time extent $t = 20$. The entire universe has collapsed into a slice of minimal time extension.

the geometry in phase B corresponds to a Euclidean geometry in the so-called crumpled phase, which is characterized by the presence of very few vertices with extremely high coordination number [15,16,26,27]. We will not elaborate here on our detailed measurements which quantify these statements, because we view phases A and B as lattice artifacts. However, there is yet another phase where the dynamics is not reduced to just the spatial directions but is genuinely four-dimensional.

(c) This phase occurs for sufficiently small κ_0 and nonvanishing asymmetry Δ. In this phase, where $\Delta > 0$ and $\tilde{\alpha} < 1$ ($\tilde{\alpha}$ was defined below Eq. (1)), there seems to be a sufficiently strong coupling between successive spatial slices to induce a change in the spatial structure itself. We will discuss this new geometrical structure in detail in Sec. VI.

Of course, the presence of the asymmetry parameter Δ is only possible because of the Lorentzian character of the model, and the resulting distinction between spatial and time directions. Since we implemented this distinction in the discretization by setting up a particular proper-time foliation and choosing arbitrary discrete length and time scales, it should not be surprising that in order to make contact with continuum physics, the ratio of these two scales cannot be chosen completely arbitrarily. This merely implies a restriction on the way the discretization is set up, and does not lead to any new parameters in the continuum theory. We have checked that the physical results derived within phase C do not depend on the numerical value of Δ, within the allowed range. As we will see later, any such choice leads to the large-scale geometry of a homogeneous and isotropic universe.

The hallmark of this phase is the presence of a stable extended four-geometry, as first reported in [19], and illustrated in Fig. 6. Not only does the macroscopic dimensionality of spacetime emerge with the correct classical value, but, equally remarkably, the global shape of the universe has been shown to be related to a simple minisuperspace action similar to those used in standard quantum cosmology [20]. Details of the computer measurements in this phase are the subject of Secs. V, VI, and VII below.

Looking at the phase diagram of Fig. 3, it may at first be surprising that one does not obtain a continuum limit when the bare gravitational coupling constant (or Newton's constant) vanishes, $G^{(b)} \sim 1/k^{(b)} \to 0$. However, one should bear in mind that the method of dynamical triangulation is a way of defining the path integral, rather than a regularization method which has nice smooth continuum manifolds as its dominant configurations as $G^{(b)} \to 0$.

A helpful analogy is the example of the (Euclidean) path integral for the relativistic particle, whose propagator $G(x, y)$ can be represented as a sum over all random paths from x to y, whose action $S(P) = m^{(b)}L(P)$ is given by the length L of the path P in target space, multiplied by a dimensionless bare mass parameter $m^{(b)}$. If this path integral is regularized on a hypercubic lattice in R^d, the possible paths are by definition along the lattice links. Now

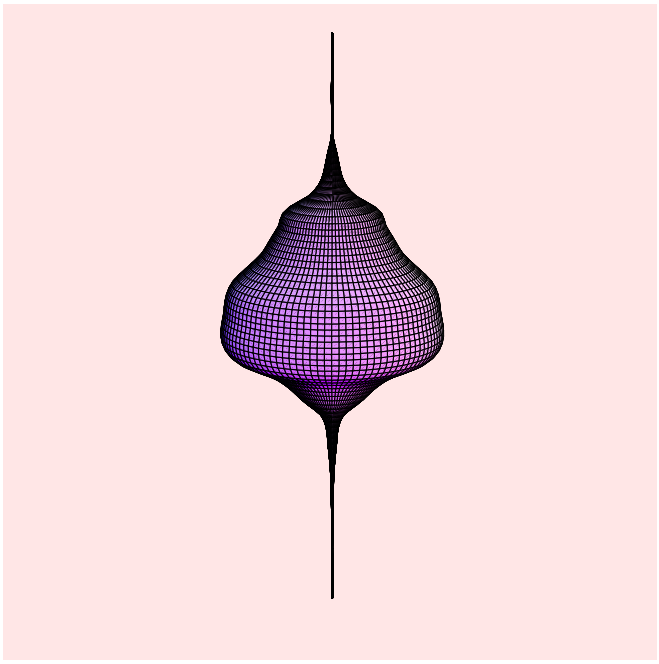

FIG. 6 (color online). Monte Carlo snapshot of a typical universe in phase C ($\kappa_0 = 2.2$) of discrete volume $N_4 = 91.1$ k and total time extent $t = 40$.

consider R^2 and a path from $(0, 0)$ to the lattice point $(x, y) = (a \cdot n, a \cdot n)$. No matter how small the lattice spacing a and how large the number n of lattice steps, the lattice paths between the two points will never approach smooth continuum paths and their lengths will always be larger than $\sqrt{2}\sqrt{x^2 + y^2}$. To define a continuum limit for the lattice random walk one looks for critical points of the corresponding statistical system and studies the long-distance properties of suitable observables, in this case, of the propagator. The critical point is determined by the value of $m^{(b)}$, but this bare coupling constant is usually not related to the physical parameter (given here by the mass term in the continuum propagator) in a straightforward way (see [18,28]) for details). In the case of dynamical triangulations we follow a similar strategy. We do not *a priori* associate a continuum limit with certain values of the bare coupling constants. Rather, we look for points or regions in coupling-constant space where interesting scaling limits may exist. In the case of four-dimensional gravity, it is natural to look for regions where some desirable features of macroscopic spacetime are reproduced, and this is precisely the case for the phase-space region (C).

Let us also comment on how the continuum limit is taken in our approach. According to the standard, Wilsonian understanding of the relation between the theory of critical phenomena in statistical mechanics and quantum field theory, in order to obtain a continuum quantum field theory from an underlying regularized statistical system one needs to fine-tune a few coupling constants (corresponding to the relevant directions in coupling-constant space) to reach the infinite-dimensional critical surface where a suitably defined correlation length is infinite. Directions along the critical surface correspond to the infinitely many irrelevant (nonrenormalizable) directions in coupling-constant space. Weinberg conjectured that this picture, which is usually believed to define ordinary renormalizable quantum field theories, may generalize to quantum gravity, in the sense that it may have an associated, nonperturbatively defined critical surface [29]. Several groups have since tried to substantiate this idea using either a $(2 + \epsilon)$-expansion [30] or refined renormalization group techniques [3]. Various lattice approaches to quantum gravity like quantum Regge calculus [31], Euclidean dynamical triangulations [11,12,32] and the causal dynamical triangulation of quantum gravity [10,19,20] used by us presently also endorse this picture.

In the latter, Lorentzian approach, the bare cosmological constant must be fine-tuned to obtain an infinite spacetime volume. Formally, we are not performing an analogous fine-tuning of the bare gravitational coupling constant in phase C, which is nonstandard from a Wilsonian point of view. There *are* indeed lattice theories where no fine-tuning is needed, and where an infinite-volume limit is sufficient to identify a continuum limit, for example, the Coulomb phase of $U(1)$-lattice gauge theory. However, the situation in gravity could be more involved, and subtleties may be buried in the identification of more complicated observables than the global ones we have considered so far. For a related discussion in three-dimensional causal dynamically triangulated quantum gravity, we refer to [33,34]. What is important from our present point of view is the fact that the universes emerging from phase C satisfy the first nontrivial tests of being viable candidates for quantum universes, as we will now turn to describe. Encouraged by these results, we are in the process of developing new and more refined methods to probe the geometry of the model further, and which eventually should allow us to test aspects related to its local "transverse" degrees of freedom, the gravitons. We invite and challenge our readers to find such tests in a truly background-independent formalism of quantum gravity.

V. MEASURING GEOMETRY

Having generated a ground state of quantum geometry nonperturbatively, we would like to understand its geometric properties, in the sense of expectation values, which can be done in various ways. We will currently concentrate on the purely geometric observables, leaving the coupling to test particles and matter fields to a later investigation. We will proceed by first determining a number of "rough" properties of the quantum geometry such as its dimensionality and its global scaling properties. These properties of quantum spacetime play an important role, because for any viable candidate theory of quantum gravity, they must be shown to reproduce the correct classical limit at sufficiently large scales, namely, geometry as described by Einstein's general theory of relativity.

As we have emphasized in [19], in nonperturbative models of quantum gravity, where by definition geometry fluctuates very strongly at short scales, there is absolutely no guarantee that any sensible classical limit is obtained even for very basic quantities like the dimension of spacetime. This is at first rather surprising: how can a superposition of locally d-dimensional geometries (made from d-dimensional simplicial building blocks) give anything that is *not* again d-dimensional? The resolution to this seeming paradox is that the statements about dimensionality always have to be understood in the limit where the lattice spacing a (measuring the edge lengths of the simplices) goes to zero, while the total d-volume, defined as the number of d-simplices times a^d, stays constant.

As an explicit example consider a triangulation of a three-dimensional manifold with topology $[0, 1] \times S^2$. Represent the two-sphere by a minimal triangulation of just four triangles (which can be thought of as forming the surface of a tetrahedron), and connect two such spheres with a minimal number of three-simplices (i.e. ten tetrahedra) to obtain a three-dimensional simplicial manifold of the desired topology. Extend this space into a long chain by adjoining more S^2's, each connected to the previous one by

a set of ten tetrahedra. Clearly, if we shrink the lattice spacing a to zero while extending the chain such that the three-volume $N_3 a^3$ is constant (where N_3 denotes the total number of tetrahedra), we effectively create a one-dimensional structure although our starting point was perfectly three-dimensional. By an analogous construction one can obtain a one-dimensional space using building blocks of any dimensionality d. The opposite extreme, namely, a geometry which is effectively infinite-dimensional, can be constructed as a limit of triangulations where almost all simplices share a common vertex. In these triangulations one can move between *any* two vertices in just a few steps (moving along the edges of simplices), no matter how many d-simplices they contain. Applying then a standard definition of Hausdorff dimension, such geometries will be assigned an infinite dimension in the limit.

These examples show that there are spaces with ''exotic'' dimensionality which can be obtained as limiting cases of regular simplicial manifolds. Of course, the relevant question for the gravitational path integral is whether geometries of this nature indeed dominate the path integral in the continuum limit when the lattice spacing a goes to zero. This is a genuinely dynamical question which cannot be decided *a priori*. It depends on the relative weight of ''energy'' and ''entropy'', that is to say, the Boltzmann weight of a given geometry (which in turn is a function of the values of the bare coupling constants) *and* the number of geometries with a given, fixed Boltzmann weight. Thus it may happen that a class of highly degenerate geometries dominates over more ''normal'' geometries either because they are energetically favored or because they are more numerous. Indeed, previous formulations which can probe the dimensionality of geometry numerically through the scaling behavior of suitable observables, for example, dynamically triangulated models of Euclidean quantum gravity, have not come up with evidence for the value 4. Instead such models seem to run generically into highly degenerate geometries of one type or other [12,14,16,35], which at large scales have nothing to do with four-dimensional spacetime as we know it. From this it seems likely that the condition of obtaining the correct classical limit imposes strong constraints on any attempt to quantize gravity *nonperturbatively and background-independently*. Of course, proposals of quantizing gravity are often not sufficiently developed to decide whether they can reproduce classical geometry from first principles, without putting in a preferred background structure along the way.

In the following, we will present a detailed discussion of a number of geometric properties of the extended ground state of phase C above. Several main results were already announced in our previous publications [19–21]. The picture emerging so far is that of a geometry whose large-scale properties are classical, but whose detailed microscopic structure is highly complicated and nonclassical. We will proceed by first presenting the evidence for the macroscopic four-dimensionality of spacetime, and then describing the insights into the geometric structure obtained from measuring quantities associated with slices of constant time.

A. The evidence for spacetime dimension four: Global scaling

As illustrated by Fig. 6, the total four-volume is distributed over the t time steps (we are working with a periodic identification in the time direction) in a characteristic way. At a given discrete four-volume, for sufficiently large t the configuration separates out into a thin ''stalk'' whose four-volume at each time step fluctuates little and is close to the kinematically allowed minimum for the topology $[0, 1] \times S^3$, and an extended, blob-shaped structure, the ''universe''. The average volume s per time step $\Delta\tau = 1$ of the stalk is practically independent of the total volume of the system, with $s \approx 25.5$ for the range of coupling constants we used. As explained in Sec. III, we measure the spacetime volume by $\tilde{N}_4$, that is, in units of four-simplices of type (4,1). Since every spatial tetrahedron is contained in exactly two (4,1)-simplices, the average three-volume $N_3(\tau)$ at integer time τ in the stalk is therefore given by $s/2$.

A suitable observable for studying the large-scale structure of the universe is the volume-volume correlator[5]

$$C_{\tilde{N}_4}(\delta) \equiv \langle N_3(0) N_3(\delta)\rangle = \sum_{\tau=1}^{t} \frac{4\langle (N_3(\tau) - s/2)(N_3(\tau+\delta) - s/2)\rangle}{(\tilde{N}_4 - ts)^2}, \quad (7)$$

which satisfies the normalization condition

$$\sum_{\delta=0}^{t-1} C_{\tilde{N}_4}(\delta) = 1, \quad (8)$$

where a periodic identification of the time variable has been assumed. Because of the subtraction of the cutoff volume $s/2$, the volume-volume correlator is only sensitive to the extended part of the geometry, and measures the distribution of the ''effective'' four-volume

$$\tilde{N}_4^{\text{eff}} = \tilde{N}_4 - ts \quad (9)$$

contained in it. We have measured the distribution (7) for system sizes $\tilde{N}_4 = 10, 20, 40, 80$ and 160 k, at $\kappa_0 = 2.2$, $\Delta = 0.6$ and $t = 80$. We expect the distribution to scale as a function of $\tilde{N}_4$, with an underlying universal distribution

$$c_{\tilde{N}_4}(x) := (\tilde{N}_4^{eff})^{1/D_H} C_{\tilde{N}_4}((\tilde{N}_4^{eff})^{1/D_H} x) \quad (10)$$

[5]Note that in the analogous relation (6) in [19] we mistakenly omitted the ensemble averages on the right-hand side.

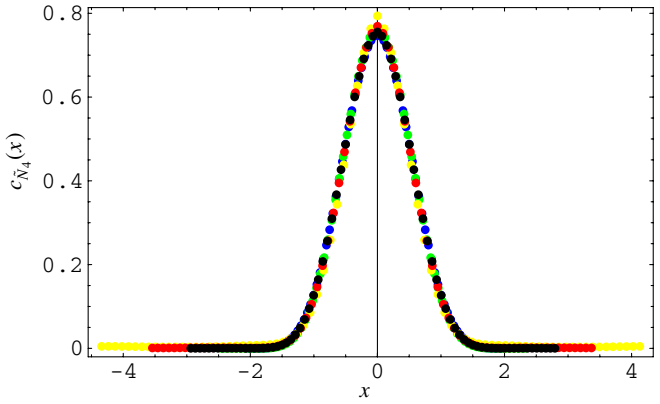

FIG. 7 (color online). The scaling of the volume-volume distribution, as function of the rescaled time variable $x = \delta/(\tilde{N}_4^{\rm eff})^{1/4}$. Data points come from system sizes $\tilde{N}_4 = 10, 20, 40, 80$ and 160 k at $\kappa_0 = 2.2$, $\Delta = 0.6$ and $t = 80$.

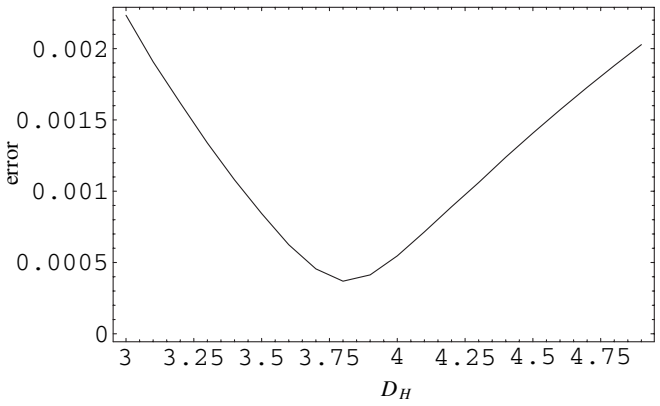

FIG. 8. Estimating the best scaling dimension D_H from optimal overlaps of rescaled volume-volume distributions. The plot variable is the average error of the overlap as function of D_H.

depending on the rescaled time variable[6]

$$x = \frac{\delta}{(\tilde{N}_4^{\rm eff})^{1/D_H}}. \tag{11}$$

The value of the scaling dimension D_H is then determined by the method of "best overlap". In it, we compare each measured distribution with that of the 40k system. In order to provide a comparison point for each value of x and to quantify the overlap, we first performed a spline interpolation of the discrete distribution at 40 k. Figure 7 shows a combined plot of the rescaled distributions, using $D_H = 4$ as a scaling dimension, and with a plot range symmetrized around $x = 0$. The overlap is nearly perfect. As can be read off Fig. 8, which shows the average error of the overlap as a function of D_H, the best overlap corresponds to $D_H \approx 3.8 \pm 0.25$. We take this outcome as strong evidence that our spacetimes are genuinely four-dimensional at large scales.[7]

B. The evidence for spacetime dimension four: Spectral dimension

Another way of obtaining an effective dimension of the nonperturbative ground state, its so-called *spectral dimension* D_S, is from studying a diffusion process on the underlying geometric ensemble. On a d-dimensional manifold with a fixed, smooth Riemannian metric $g_{ab}(\xi)$, the diffusion equation has the form

$$\frac{\partial}{\partial\sigma} K_g(\xi, \xi_0; \sigma) = \Delta_g K_g(\xi, \xi_0; \sigma), \tag{12}$$

where σ is a fictitious diffusion time, Δ_g the Laplace operator of the metric $g_{ab}(\xi)$ and $K_g(\xi, \xi_0; \sigma)$ the probability density of diffusion from ξ to ξ_0 in diffusion time σ. We will consider diffusion processes which initially are peaked at some point ξ_0,

$$K_g(\xi, \xi_0; \sigma = 0) = \frac{1}{\sqrt{\det g(\xi)}} \delta^d(\xi - \xi_0). \tag{13}$$

For the special case of a flat Euclidean metric, we have

$$K_g(\xi, \xi_0; \sigma) = \frac{e^{-d_g^2(\xi,\xi_0)/4\sigma}}{(4\pi\sigma)^{d/2}}, \qquad g_{ab}(\xi) = \delta_{ab}. \tag{14}$$

For general curved spaces K_g has the well-known asymptotic expansion

$$K_g(\xi, \xi_0; \sigma) \sim \frac{e^{-d_g^2(\xi,\xi_0)/4\sigma}}{\sigma^{d/2}} \sum_{r=0}^{\infty} a_r(\xi, \xi_0)\sigma^r \tag{15}$$

for small σ, where $d_g(\xi, \xi_0)$ denotes the geodesic distance between ξ and ξ_0. Note the appearance of the power $\sigma^{-d/2}$ in this relation, reflecting the dimension d of the manifold, just like in the formula (14) for flat space. This happens because small σ's correspond to short distances and for any given smooth metric short distances imply approximate flatness.

A quantity that is easier to measure in numerical simulations is the average *return probability* $P_g(\sigma)$, which possesses an analogous expansion for small σ,

[6]We are employing standard finite-size scaling methods familiar from the theory of critical phenomena (see [36] for a textbook exposition), adjusted to our problem.

[7]Of course, we will never be able to show by computer simulations alone that the effective dimension is exactly equal to four. What we are assuming here is that this dimension is indeed an integer, because there are no classical theories describing the dynamics of geometries of dimensionality 3.9, say. Also, it is known from the measurement of Hausdorff dimensions in two-dimensional Euclidean quantum gravity (where it can be proven that the Hausdorff dimension is four (!) [37,38]) that the computer simulations tend to slightly underestimate the actual values [39,40].

$$P_g(\sigma) \equiv \frac{1}{V}\int d^d\xi\sqrt{\det g(\xi)}K_g(\xi,\xi;\sigma) \sim \frac{1}{\sigma^{d/2}}\sum_{r=0}^{\infty} A_r\sigma^r, \tag{16}$$

where V is the spacetime volume $V = \int d^d\xi\sqrt{\det g(\xi)}$ and the expansion coefficients A_r are given by

$$A_r = \frac{1}{V}\int d^d\xi\sqrt{\det g(\xi)}a_r(\xi,\xi). \tag{17}$$

For an infinite flat space, we have $P_g(\sigma) = 1/(4\pi\sigma)^{d/2}$ and thus can extract the dimension d by taking the logarithmic derivative,

$$-2\frac{d\log P_g(\sigma)}{d\log\sigma} = d, \tag{18}$$

independent of σ. For nonflat spaces and/or finite volume V, one can still use Eq. (18) to extract the dimension, but there will be corrections for sufficiently large σ. For finite volume, in particular, $P_g(\sigma)$ goes to $1/V$ for $\sigma \gg V^{2/d}$ since the zero mode of the Laplacian $-\Delta_g$ will dominate the diffusion in this region. For a given diffusion time σ the behavior of $P_g(\sigma)$ is determined by eigenvalues λ_n of $-\Delta_g$ with $\lambda_n \leq 1/\sigma$, and the contribution from higher eigenvalues is exponentially suppressed. Like in the flat case, where diffusion over a time σ probes the geometry at a linear scale $\sqrt{\sigma}$, large σ corresponds to large distances away from the origin ξ_0 of the diffusion process, and small σ to short distances.

The construction above can be illustrated by the simplest example of diffusion in one dimension. The solution to the diffusion equation on the real axis is

$$K(\xi,\sigma) = \frac{e^{-\xi^2/4\sigma}}{\sqrt{4\pi\sigma}}, \qquad K(k,\sigma) = e^{-k^2\sigma}, \tag{19}$$

where $K(k,\sigma)$ denotes the Fourier transform of $K(\xi,\sigma)$. The eigenvalues of the Laplace operator are of course just given by k^2. In order to illustrate the finite-volume effect, let us compactify the real line to a circle of length L. The return probability is now given by

$$P_L(\sigma) = \frac{1}{L}\sum_{n=-\infty}^{\infty} e^{-k_n^2\sigma} = \frac{1}{\sqrt{4\pi\sigma}}\sum_{m=-\infty}^{\infty} e^{-L^2m^2/4\sigma}, \qquad k_n = \frac{2\pi n}{L}, \tag{20}$$

where in the second step we have performed a Poisson resummation to highlight the $\sigma^{-1/2}$-dependence for small σ. In line with the discussion above, the associated spectral dimension $D_S(\sigma)$ is constant (and equal to one) up to σ-values of the order $L^2/4\pi^2$, and then goes to zero monotonically.

In applying this set-up to four-dimensional quantum gravity in a path-integral formulation, we are interested in measuring the expectation value of the return probability $P_g(\sigma)$. Since $P_g(\sigma)$ defined in (16) is invariant under reparametrizations, it makes sense to take its quantum average over all geometries of a given spacetime volume V_4,

$$P_{V_4}(\sigma) = \frac{1}{\tilde{Z}_E(V_4)}\int \mathcal{D}[g_{ab}]e^{-\tilde{S}_E(g_{ab})}\delta\Big(\int d^4x\sqrt{\det g} - V_4\Big) \times P_g(\sigma), \tag{21}$$

where the partition function $\tilde{Z}_E$ and the corresponding gravitational action $\tilde{S}_E$ were defined in (4). Since the small-σ behavior of $P_g(\sigma)$ is the same for each smooth geometry, it might seem obvious that the same is true for their integral $P_{V_4}(\sigma)$, but this need not be so. Firstly, the scale σ in (21) is held fixed, independent of the geometry g_{ab}, while the expansion (16) contains reference to higher powers of the curvature of g_{ab}. Secondly, one should keep in mind that a typical geometry which contributes to the path integral—although continuous—is unlikely to be smooth. This does not invalidate our treatment, since diffusion processes can be meaningfully defined on much more general objects than smooth manifolds. For example, the return probability for diffusion on fractal structures is well studied in statistical physics and takes the form

$$P_N(\sigma) = \sigma^{-D_S/2}F\Big(\frac{\sigma}{N^{2/D_S}}\Big), \tag{22}$$

where N is the "volume" associated with the fractal structure and D_S the so-called *spectral dimension*, which is not necessarily an integer. An example of fractal structures are branched polymers (which will play a role in Sec. VI below when we analyze the geometry of spatial slices), which generically have $D_S = 4/3$ [41,42]. Extensive numerical simulations [43,44,65] have shown that in 2d quantum gravity the only effect of integrating over geometries is to replace the asymptotic expansion (16), which contains reference to powers of the curvature related to a specific metric, by the simpler form (22).

Our next task is to define diffusion on the class of metric spaces under consideration, the piecewise linear structures defined by the causal triangulations T. We start from an initial probability distribution

$$K_T(i, i_0; \sigma = 0) = \delta_{i,i_0}, \tag{23}$$

which vanishes everywhere except at a randomly chosen (4,1)-simplex i_0, and define the diffusion process by the evolution rule

$$K_T(j, i_0; \sigma + 1) = \frac{1}{5}\sum_{k\to j} K_T(k, i_0; \sigma). \tag{24}$$

These equations are the simplicial analogues of (13) and (12), with the triangulation (together with its Euclideanized edge-length assignments) playing the role of g_{ab}, and $k \to j$ denoting the five nearest neighbors of the four-simplex j. In this process, the total probability

$$\sum_j K_T(j, i_0; \sigma) = 1 \tag{25}$$

is conserved. The return probability to a simplex i_0 is then defined as $P_T(i_0; \sigma) = K_T(i_0, i_0; \sigma)$ and the quantum average as

$$P_{N_4}(\sigma) = \frac{1}{\tilde{Z}_E(N_4)} \sum_{T_{N_4}} e^{-\tilde{S}_E(T_{N_4})} \frac{1}{N_4} \sum_{i_0 \in T_{N_4}} K_{T_{N_4}}(i_0, i_0; \sigma), \tag{26}$$

where T_{N_4} denotes a triangulation with N_4 four-simplices, and $\tilde{S}_E(T_{N_4})$ and $\tilde{Z}_E(N_4)$ are the obvious simplicial analogues of the continuum quantities (4) at fixed four-volume. Assuming that the return probability behaves according to (22), with $N = N_4$, we can extract the value of the fractal dimension D_S by measuring the logarithmic derivative as in (18) above, as long as the diffusion time is not much larger than N_4^{2/D_S},

$$D_S(\sigma) = -2 \frac{d \log P_{N_4}(\sigma)}{d \log \sigma} + \text{finite-size corrections.} \tag{27}$$

From the experience with numerical simulations of 2d Euclidean quantum gravity in terms of dynamical triangulations [40,43,44,65], we expect some irregularities in the behavior of the return probability for the smallest σ, i.e. close to the cut-off scale. Typically, the behavior of $P_N(\sigma)$ for odd and even diffusion steps σ will be quite different for small σ and merge only for $\sigma \approx 20 - 30$. After the merger, the curve enters a long and stable regime where the right-hand side of (27) is independent of σ, before finite-size effects start to dominate which force it to go to zero. (Also the 3d Euclidean hypersurfaces of constant time in our current set-up show a very similar behavior, as can be seen in Fig. 15.)

The origin of the odd-even asymmetry can again be illustrated by the simple case of diffusion on a one-dimensional circle, whose solution is the discretized version of the solution (20). In this case the asymmetry of the return probability between odd and even time steps is extreme: if we use the two-dimensional version of the simple evolution Eq. (24), we obtain

$$P_L(\sigma) = \begin{cases} 0 & \text{for } \sigma \text{ odd,} \\ \frac{1}{2^\sigma} \binom{\sigma}{\sigma/2} & \text{for } \sigma \text{ even,} \end{cases} \tag{28}$$

as long as $\sigma < L/2$, where L is the discrete volume of the circle (i.e. the number of its edges). It is of course possible to eliminate this asymmetry by using an "improved" discretized diffusion equation, but in the case of higher-dimensional random geometries like the ones used in 4d causal dynamical triangulations this is not really necessary. The random connectivity will eliminate the asymmetry after a number of steps as exemplified by Fig. 15.

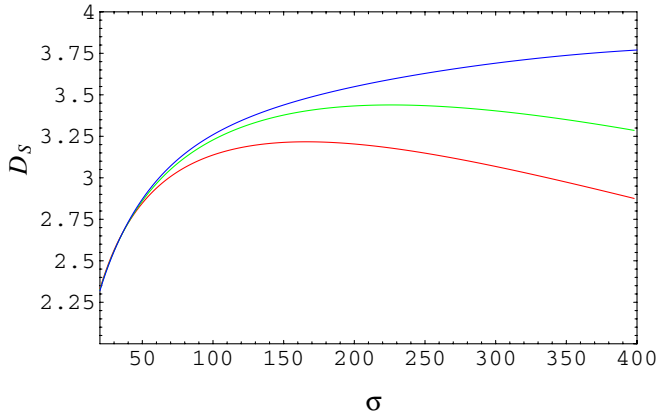

FIG. 9 (color online). The spectral dimension $D_S(\sigma)$ of causal dynamical triangulations as a function of the diffusion time σ, which is a direct measure of the distance scale probed. The measurements were taken at volumes $\tilde{N}_4 = 20$ k (bottom curve), 40 k and 80 k (top curve), and for $\kappa_0 = 2.2$, $\Delta = 0.6$ and $t = 80$.

The results of measuring the spacetime spectral dimension D_S were first reported in [21]. We work with system sizes of up to $\tilde{N}_4 = 80$k with $\kappa_0 = 2.2$, $\Delta = 0.6$ and $t = 80$. Since we are interested in the bulk properties of quantum spacetime and since the volume is not distributed evenly in the time direction (cf. Figure 6), we always start the diffusion process from a four-simplex adjacent to the slice of maximal three-volume. When this is done the variations in the curve $D_S(\sigma)$ for different generic choices of T_N and starting simplices i_0 are small. The data curves presented in Fig. 9 were obtained by averaging over 400 different diffusion processes performed on independent configurations. Because following the diffusion out to a time $\sigma = 400$ is rather time-consuming and the variation in $P_T(i_0; \sigma)$ as a function of T and i_0 (with the initial conditions specified above) is small, we have not performed a more extensive average over configurations. We have omitted error bars from Fig. 9 to illustrate how the curves converge to a shape that represents $D_S(\sigma)$ in the infinite-volume limit, and which is given by the envelope of the data curves for finite volume. For the two lower volumes, $\tilde{N}_4 = 20$ k and $\tilde{N}_4 = 40$ k, there still are clear finite-volume effects for large diffusion times σ.

By contrast, the top curve—corresponding to the maximal volume $\tilde{N}_4 = 80$ k—continues to rise for increasing σ, which makes it plausible that we can ignore any finite-size effects and that it is a good representative of the infinite-volume limit in the σ-range considered.[8] We will therefore concentrate on analysing the shape of this curve,

[8]In both Figs. 9 and 10 we have only plotted the region where the curves for odd and even σ coincide, in order to exclude short-distance lattice artifacts. The two curves merge at about $\sigma = 40$. Since the diffusion distance grows as $\sqrt{\sigma}$, a return diffusion time of 40 corresponds to just a few steps away from the initial four-simplex.

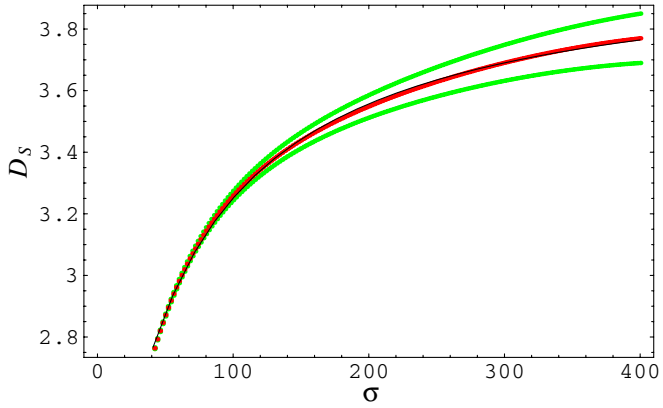

FIG. 10 (color online). The spectral dimension D_S of the universe as function of the diffusion time σ, measured for $\kappa_0 = 2.2$, $\Delta = 0.6$ and $t = 80$, and a spacetime volume $N_4 = 181$ k. The averaged measurements lie along the central curve, together with a superimposed best fit $D_S(\sigma) = 4.02 - 119/(54 + \sigma)$. The two outer curves represent error bars.

which is presented separately in Fig. 10, now with error bars included. (More precisely, the two outer curves represent the envelopes to the tops and bottoms of the error bars.) The error grows linearly with σ, due to the occurrence of the $\log\sigma$ in (27).

The remarkable feature of the curve $D_S(\sigma)$ is its slow approach to the asymptotic value of $D_S(\sigma)$ for large σ. As emphasized in [21], this type of behavior has never been observed previously in systems of random geometry, and again underlines that causal dynamical triangulations in four dimensions behave qualitatively differently, and that the quantum geometry produced is in general richer. The new phenomenon we observe here is a *scale dependence of the spectral dimension*, which has emerged dynamically. This is to be contrasted with fractal structures which show a self-similar behavior at all scales, and which lead to $D_S(\sigma)$-curves like that shown in Fig. 15.

As explained in [21], the best three-parameter fit which asymptotically approaches a constant is of the form

$$D_S(\sigma) = a - \frac{b}{\sigma + c} = 4.02 - \frac{119}{54 + \sigma}. \tag{29}$$

The constants a, b and c have been determined by using the full data range $\sigma \in [40\,400]$ and the curve shape agrees well with the measurements, as can be seen from Fig. 10. Integrating (29) we obtain

$$P(\sigma) \sim \frac{1}{\sigma^{a/2}(1 + c/\sigma)^{b/2c}}, \tag{30}$$

from which we deduce the limiting cases

$$P(\sigma) \sim \begin{cases} \sigma^{-a/2} & \text{for large } \sigma, \\ \sigma^{-(a-b/c)/2} & \text{for small } \sigma. \end{cases} \tag{31}$$

We conclude that the quantum geometry generated by causal dynamical triangulations has a scale-dependent spectral dimension which increases continuously from $a - b/c$ to a with increasing distance. Substituting the values for a, b and c obtained from the fit (29), and taking into account their variation as we vary the σ-range $[\sigma_{\min}, \sigma_{\max}]$ and use different weightings for the errors, we obtained the asymptotic values [21]

$$D_S(\sigma = \infty) = 4.02 \pm 0.1 \tag{32}$$

for the "long-distance spectral dimension" and

$$D_S(\sigma = 0) = 1.80 \pm 0.25 \tag{33}$$

for the "short-distance spectral dimension". A dynamically generated scale-dependent dimension with this behavior is truly exciting news, because it signals the existence of an effective ultraviolet cut-off for theories of gravity with and without matter coupling, brought about by the (highly nonperturbative) behavior of the quantum-geometric degrees of freedom on the very smallest scale.

C. The effective action

In order to get a more detailed understanding of the geometric properties of our universe, we next attempt to reproduce the overall shape of the universe of Fig. 6 (in other words, the behavior of its three-volume V_3 as a function of time) from an effective action for the single variable $V_3(\tau)$, valid at sufficiently large scales $V_3 \gg 1$. This will enable us to compare our results with those from so-called minisuperspace models. The simplest such models also take the form of dynamical systems of a single variable, namely, the scale factor $a(\tau)$, describing the linear spatial extension of the universe and related to the three-volume by

$$V_3(\tau) \propto a^3(\tau). \tag{34}$$

Despite the resemblance, the status of our derivation is very different from that of a minisuperspace model. In the latter, one works from the outset in a drastically truncated framework, where the classical dynamics of the entire universe is described by the variable $a(\tau)$ instead of the full metric data $g_{ij}(\tau, x)$. For closed universes, and in (Euclidean) proper-time coordinates, this corresponds to considering line elements of the form

$$ds^2 = d\tau^2 + a^2(\tau) d\Omega_3^2, \tag{35}$$

where $d\Omega_3^2$ denotes the metric on the three-sphere. The corresponding Einstein-Hilbert action[9] is

$$S^{\min} = \frac{1}{G} \int d\tau \left(-a(\tau) \left(\frac{da(\tau)}{d\tau} \right)^2 - a(\tau) + \lambda a^3(\tau) \right), \tag{36}$$

[9]We work with Euclidean signature in order to facilitate comparison with the simulation data, which also describe Euclidean, Wick-rotated geometries.

including a cosmological constant λ. These minisuperspace models are often taken as starting point for a path-integral quantization, leading to quantum cosmologies like those used by Hartle and Hawking in their semiclassical evaluation of the wave function of the universe [45] (see also [46–53] for related work). The hope is that such a truncated version of quantum gravity still describes some features of the full theory correctly.

By contrast, the central feature of dynamical triangulations is a bona fide path integration over *all* geometric degrees of freedom (which, in particular, will have a nontrivial spatial dependence), without appealing to any symmetry reduction, either classical or quantum-mechanical. In the final result, one may then decide to keep track only of the three-volume (equivalently, the scale factor) as a dynamical variable and try to extract its effective large-scale behavior. It is an interesting question whether the two approaches (that is, truncating the degrees of freedom before or after the quantization) are equivalent. In view of the severe difficulties in making quantum-cosmological path integrals well-defined and convergent [51], one might hope that they are not. This is indeed the conclusion from the findings in causal dynamical triangulations we are about to describe. As we will see, the collective effect of the full quantum-gravitational degrees of freedom changes the dynamical description in terms of the single scale factor in a drastic way.

Our first step is to determine the kinetic term in the effective action of the dynamically triangulated model, and compare it to the term $-a\dot{a}^2$ of the minisuperspace model (36). We obtain this term by measuring the distribution of differences of adjacent spatial volumes

$$z = \frac{|N_3(\tau+1) - N_3(\tau)|}{N_3^{1/D_2}}, \qquad N_3 = N_3(\tau) + N_3(\tau+1). \tag{37}$$

for different values of the discrete three-volume N_3. Again, the information we extract is two-fold: we first determine the exponent D_2 from best overlap, and subsequently the overall shape of the universal distribution. In order to maximize the sampled three-volumes, we employ the free boundary conditions described in Sec. III above. That is, all configurations extend over three time steps, $\Delta\tau = 3$, with only a single vertex each at the initial time $\tau = 0$ and the final time $\tau = 3$, and the relevant volume difference given by (37), with $\tau = 1$. From taking measurements at system volumes $\tilde{N}_4 = 10, 20, 40, 80$ and 160 k, we extracted a best value for D_2 by minimizing the failure of the curves to overlap for different volumes, using the same method described earlier for the determination of the scaling dimension D_H. The result is illustrated by the curve of Fig. 11 which has its minimum at about 2.12, which we interpret as evidence for $D_2 = 2$. The overlapping curves for the volume distributions $P_{N_3}(z)$ at $D_2 = 2$ are depicted in Fig. 12. Apart from z-values near zero, the overlap is clearly good. Moreover, the curve is fitted very well by a Gaussian e^{-cz^2}, with a positive constant c independent of N_3.

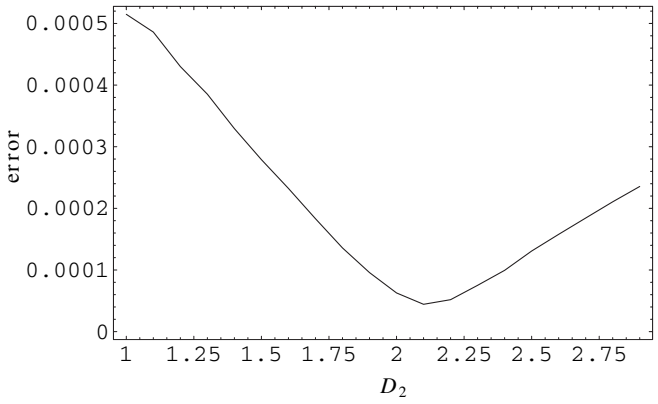

FIG. 11. Extracting the scaling dimension D_2 by finite-size scaling, in order to determine the kinetic term in the effective action of the scale factor.

From estimating the entropy of spatial geometries, that is, the number $\mathcal{N}(N_3)$ of three-dimensional configurations at given three-volume N_3, one expects [27] corrections of the form $-c'N_3^\alpha$, with $0 \le \alpha < 1$, $c' > 0$, to the exponent $-cz^2 \equiv -c(\Delta N_3/\Delta\tau)^2/N_3$ in the distribution $P_{N_3}(z)$. This leads us to the following form for the Euclidean effective action, *valid for large three-volume* $N_3(\tau)$,

$$S_{N_4}^{\text{eff}} \propto \sum_{\tau=0}^{t}\left(\frac{c_1}{N_3(\tau)}\left(\frac{\Delta N_3(\tau)}{\Delta\tau}\right)^2 + c_2 N_3^\alpha(\tau) - \lambda N_3(\tau)\right), \tag{38}$$

with $0 \le \alpha < 1$, and $c_1, c_2 > 0$. In (38), λ is a Lagrange multiplier to be determined such that

$$\sum_{\tau=0}^{t} N_3(\tau) = N_4. \tag{39}$$

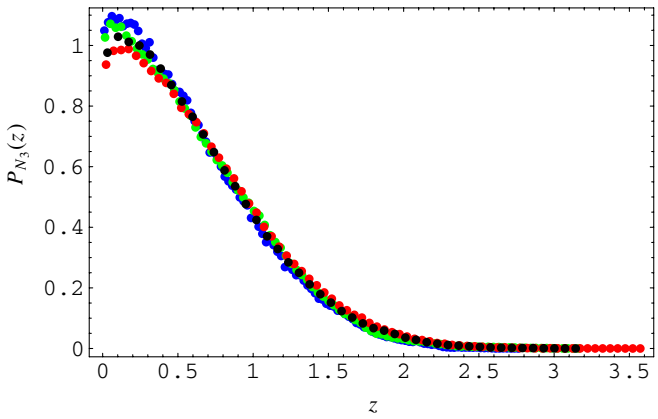

FIG. 12 (color online). The distribution $P_{N_3}(z)$ of rescaled volume differences z between adjacent spatial slices, for three-volumes $N_3 = 20, 40, 80$ and 160 k.

Unfortunately it is impossible to measure the precise form of the correction term $c_2 N_3^\alpha$ directly in a reliable way. However, it is clear from a general scaling of the above action that the only possibility for obtaining the observed scaling law, expressed in terms of the variable $\tau/N_4^{1/4}$, is by setting $\alpha = 1/3$.[10]

Reverting back to a formulation in terms of the scale factor $a(\tau)$, and by suitable rescaling of τ and $a(\tau)$), we can now write the effective action of causal dynamical triangulations at fixed continuum four-volume V_4 as

$$S^{\rm eff}_{V_4} = \frac{1}{G}\int_0^t d\tau \left(a(\tau)\left(\frac{da(\tau)}{d\tau}\right)^2 + a(\tau) - \lambda a^3(\tau)\right). \quad (40)$$

Again, this expression is valid for sufficiently large-scale factor, since we have explicitly dropped any reference to the quantum corrections at small a. Comparing now with (36), the startling conclusion is that we have indeed rederived the Euclidean minisuperspace action. However, here we have done it from first principles, and *up to an overall sign*. The strongest evidence so far that the effective action is indeed given by (40) comes from using it as *input* to create an artificial distribution of three-volumes $N_3(\tau)$ [20]. We then evaluate the volume-volume correlator $c_{\tilde{N}_4}(x)$ of Eq. (10) on this ensemble in the same way as we would do for genuine Monte Carlo data. As illustrated in Fig. 13, the matching of this new curve with the previous Monte Carlo results (c.f. Fig. 7) is impressive.

One immediate conclusion is that the collective effect of the dynamical degrees of freedom other than $a(\tau)$, which are ignored in minisuperspace models, is to change the sign of the kinetic term for the scale factor (the ''global conformal mode'') from $-a\dot{a}^2$ to $+a\dot{a}^2$. This is the same nonperturbative cure of the conformal divergence of the Euclidean path integral already encountered in dimension 3 [54,55] and argued for from a continuum point of view in [56]. It provides further evidence that the well-known sicknesses and ambiguities of the Euclidean path-integral approach are features of the semiclassical and symmetry-reduced approximations, not shared by a full nonperturbative treatment which is rooted in a causal, Lorentzian formulation.

We have begun an exploration of the consequences of our result for cosmology and quantum cosmology. When searching for a physical interpretation, one must keep in mind that the effective action (40) we extracted directly from the computer simulations holds for fixed four-volume. Translating between propagators of fixed four-volume and fixed cosmological constant requires a further Laplace transformation [20]. Moreover, we are still in the Euclidean sector of the theory, and must Wick-rotate back to obtain physical, Lorentzian results.

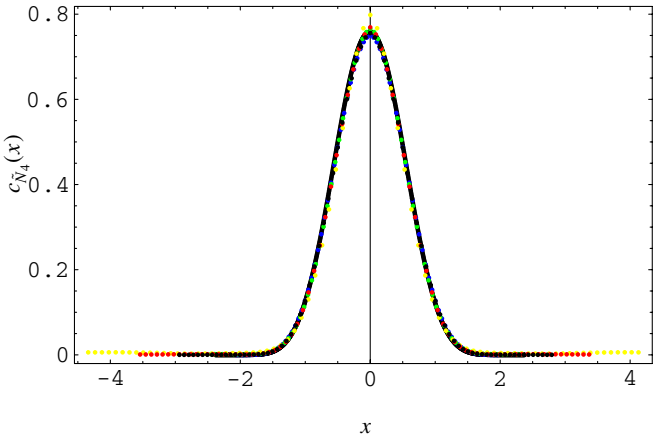

FIG. 13 (color online). The scaling of the volume-volume distribution, as function of the rescaled time variable $x = \delta/(\tilde{N}_4^{\rm eff})^{1/4}$, taken from Fig. 7, but now superimposed with the correlator obtained when using the minisuperspace action (40) to generate a distribution of three-geometries (black curve).

Nevertheless, it is exciting to see that the computation of some physical quantities is already within reach:, for example, we showed in [20] how to derive the semiclassical wave function of the universe without explicitly performing an inverse Wick rotation. The wave function can be compared directly with those arising in standard minisuperspace treatments, like those of Vilenkin [47,53], Hawking [45,46] and Linde [48]. To relate to the dynamics of the real universe, especially at very early times, we will need to couple matter to our causal geometries. These issues are currently being investigated and will be reported in the near future.

VI. NONCLASSICAL STRUCTURE OF THE UNIVERSE: THE GEOMETRY OF SPATIAL SLICES

Having established that our quantum universe possesses certain classical features at sufficiently large scales, we are interested in a more detailed characterization of its geometry. We report in this section on various measurements associated with the geometry of spatial slices $\tau = const$, and in the next section on that of ''thick spatial slices'', by which we mean geometries of time extension $\Delta\tau = 1$, which are ''sandwiched'' between adjacent spatial slices of integer-time τ. Our measurements describe certain invariant geometric properties of the ground state of spacetime, but we make at this stage no attempt to relate them to actual observables that one could go out and measure in the real universe. They will merely serve to illustrate the complexity of the geometric structure and highlight some of its nonclassical features.

Because our universes have a well-defined global notion of (proper) time τ, it is relatively straightforward to per-

[10]In order to correctly reproduce the dynamics for small three-volume, namely, the stalk observed at large times τ, the function $N_3^{1/3}$ in (38) with $\alpha = 1/3$ must be replaced by a function of N_3 whose derivative at 0 goes like N_3^ν, $\nu \geq 0$, as explained in [20]. A simple choice is the replacement $N_3^{1/3} \to (1 + N_3)^{1/3} - 1$.

form measurements within a slice of constant τ. We first restrict ourselves to slices S of integer-τ. Such slices consist entirely of spatial tetrahedra (whose edges are all spacelike). The slices are of the form of spatial interfaces of topology S^3 between adjacent sandwiches made out of four-simplices. As we will see, the Hausdorff dimension of the slices turns out to be three, as one would have naively expected in a four-dimensional universe. However, the slice does not behave three-dimensionally under diffusion, and we will see that its structure is fractal in a precise sense which will be described below.

A. Hausdorff dimension

Our algorithm for determining the Hausdorff dimension d_h of the spatial slices is as follows [11]. From a given S of discrete volume N_3, we randomly pick a tetrahedron i_0. From i_0, we move out by one step and obtain $n(1)$ tetrahedra at distance 1 from i_0 (that is, its nearest neighbors). Moving out by a further step, there will be $n(2)$ tetrahedra at distance 2, and so on until all tetrahedra have been visited. The numbers $n(r)$ recorded for each distance r sum up to

$$\sum_{r=0}^{r_{\max}} n(r) = N_3. \tag{41}$$

Finally, we measure the average linear extension

$$\langle r \rangle = \frac{1}{N_3} \sum_r r n(r) \tag{42}$$

of the spatial slice. For a slice of volume N_3, this process is repeated $N_3/50 + 1$ times with different randomly chosen initial tetrahedra. The expectation value $\langle r \rangle$ is then averaged over these measurements. In this way, we obtain for every slice a data pair

$$\{\langle\langle r \rangle\rangle, N_3\}, \tag{43}$$

representing one ''bare'' measurement.

This process is performed for all t spatial slices of the geometry, thus collecting t data pairs. We have typically done this for about 1000 different spacetime geometries, obtaining altogether $1000t$ measurement points. The final results are sorted by their $\langle\langle r \rangle\rangle$-value (in practice a continuous variable) and averaged over a sequence of 100 consecutive points. This reduces the number of data points to $10t$, which are then displayed on a log-log plot. In the presence of finite-size scaling, we expect them to follow a

[11] In order to obtain good values for the Hausdorff dimension, as defined below, it is important to use that space is isotropic. This is the case for the spatial slices. However, it is obviously not really the case for the whole spacetime, where we have a bulk region and a stalk region. Thus for the measurement of the macroscopic dimensionality D_H of spacetime the scaling method described above is superior to the use of the Hausdorff dimension.

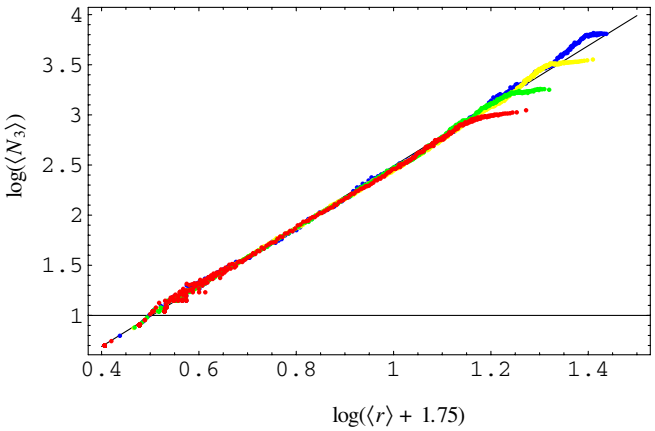

FIG. 14 (color online). Log-log plot of the average linear geodesic size $\langle r \rangle_{N_3}$ versus the three-volume N_3, measured for $\Delta = 0.4$. The straight line corresponds to a Hausdorff dimension $d_h = 3$. Similar measurements for $\Delta = 0.5$ and 0.6 yield virtually indistiguishable results.

curve

$$\langle N_3 \rangle(r) \propto (\langle r \rangle + r_0)^{d_h}, \tag{44}$$

defining a spatial Hausdorff dimension d_h. In relation (44), we have included a finite shift r_0 of the linear size r, based on earlier experience with finite-size corrections in the scaling relations [40,44]. Our results, which show universal behavior and scaling, are presented in Fig. 14. The shift value $r_0 = 1.75$ gives the best linear fit. The resulting value of $d_h \approx 3$ is practically independent of r_0.

B. Spectral dimension

Given the results of the previous sections, one might be tempted to conclude that the geometry of our dynamically generated ground state simply *is* that of a smooth four-dimensional classical spacetime, up to Gaussian fluctuations. A more detailed analysis of the geometry of spatial slices makes explicit that this is not so. We start by measuring the spectral dimension d_s of the spatial slices by studying diffusion on them. Analogous to the four-dimensional case described in Sec. V B, we choose an initial probability distribution

$$K_T(i, i_0; \sigma = 0) = \delta_{i,i_0} \tag{45}$$

on the three-dimensional triangulation T of the slice S, which is zero everywhere except at a randomly chosen tetrahedron i_0, and define the evolution in discrete time σ by the rule

$$K_T(j, i_0; \sigma + 1) = \frac{1}{4} \sum_{k \to j} K_T(k, i_0; \sigma), \tag{46}$$

where $k \to j$ labels the (four) nearest neighbors of the tetrahedron j. We measure the return probability $P_T(i_0; \sigma) = K_T(i_0, i_0; \sigma)$. The measurements of the return

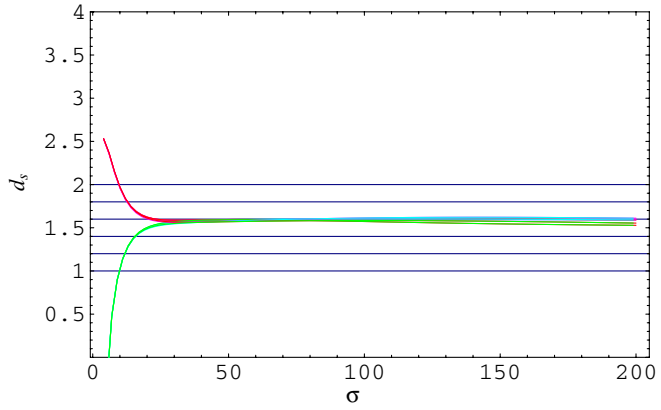

FIG. 15 (color online). The logarithmic derivative of the return probability for $\kappa_0 = 2.2$ and $\Delta = 0.4$, and spatial volumes N_3 between 500 and 2000. The measurement was performed for a system with $N_4 = 91.1k$ and $t = 40$. The increasing and decreasing lines correspond to even and odd times, and illustrate the different behavior for short diffusion times σ.

probabilities are repeated a number of times for each slice S with different starting points i_0, precisely as in the measurement of the Hausdorff dimension of S. They are then repeated for independent configurations (four-dimensional triangulations generated by the Monte Carlo-procedure), again with the same statistics as in the measurement of the Hausdorff dimension of the three-dimensional spatial slices. Results are stored for averaged slices with volumes $N_3 = n \times 500 \pm 50$, because we expect them to depend on the system volume. In this way we define the average return probability $P_{N_3}(\sigma)$ and extract the spectral dimension

$$d_s(\sigma) = -2\frac{d\log P_{N_3}(\sigma)}{d\log\sigma} \tag{47}$$

from the logarithmic derivative exactly as in the four-dimensional diffusion process.

The result is displayed in Fig. 15 for even and odd times separately, because of the different behavior of $P_{N_3}(\sigma)$ for short evolution times. As can be seen the result is very stable for larger diffusion times and gives $d_s = 1.56 \pm 0.1$ for the spectral dimension, which is only about half the expected "classical" value!

C. Critical exponents

The noncanonical value of the spatial spectral dimension shows that the quantum geometry has a nontrivial microstructure, which definitely is not that of a smooth four-dimensional manifold. In fact, we already have come across further evidence of this fact in the measurement of the spacetime spectral dimension which approached the value four only at long distances. One way to obtain an additional characterization of geometries at a fixed time is through the functional form of their entropy or "number of states" $\mathcal{N}(N)$ as function of their discrete volume N. Two different functional forms for the entropy have appeared in previous studies of simplicial *three*-dimensional quantum gravity [27], namely,

$$\mathcal{N}(N_3) \propto N_3^{-3+\gamma_{str}} e^{\mu_0 N_3}, \tag{48}$$

$$\mathcal{N}(N_3) \propto e^{\mu_0 N_3 - c_1 N_3^{\nu} + \cdots}, \quad \nu < 1, \tag{49}$$

with a nonuniversal constant μ_0 measuring the leading exponential growth. The critical exponent $\gamma_{\rm str}$ in (48) characterizes the fractal structure of the geometry [57–59]. The larger the value of $\gamma_{\rm str}$, the more pronounced the tendency for a given three-geometry to develop so-called baby universes[12].

The functional form (49) on the other hand indicates a suppression of baby universes and formally may be seen as the limit $\gamma_{\rm str} \to -\infty$ of (48). Below we will meet both functional forms. It is important to understand that the entropy $\mathcal{N}(N_3)$ in (48) and (49) does not merely count the possible three-geometries, but also includes the weight coming from the action: in counting geometries we are making an importance sampling where the action defines the probability weight of the geometry. We saw above that the choice of bare coupling constants in the four-dimensional theory determines in which of the different phases of the lattice theory we end up. The entropy of the spatial geometries at fixed time is different in the three phases, even if the underlying geometries are identical, and simply given by the space of all (abstract) triangulations of S^3.

If the functional form of the entropy is given by Eq. (48), a convenient way of measuring the exponent $\gamma_{\rm str}$ is through the distribution of baby universes [58,59]. Calling B the volume of the baby universe (the number of tetrahedra contained in it) and N_3 the total volume of the spatial geometry, we expect a distribution of the form [58,59]

$$P(x) \propto x^{-2+\gamma_{\rm str}}\left(1 + \frac{c(N_3)}{x} + \cdots\right), \tag{50}$$

where

$$x = \frac{B}{N_3}\left(1 - \frac{B}{N_3}\right), \qquad 0 < x < 1/4, \tag{51}$$

and $c(N_3) \propto 1/N_3$ is a volume-dependent constant. Relation (50) is expected to hold for sufficiently large B. (It was derived under the assumption that the samples of

[12]In the present context, a "baby universe" is a part of the three-dimensional spatial triangulation which is connected to the remainder by a "minimal neck". This means that the interface between the triangulated baby universe and the "parent universe" is topologically a sphere and of minimal size. Equivalently, it is given by the surface of a tetrahedron consisting of four triangles. This is easier to visualize in a two-dimensional simplicial manifold where the analogous minimal neck is an S^1 consisting of three edges.

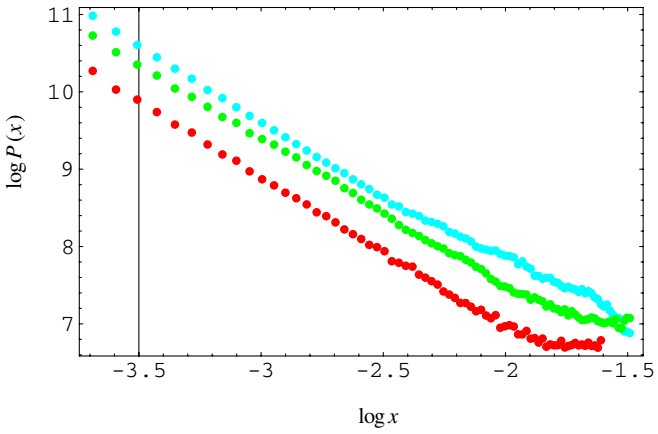

FIG. 16 (color online). The distribution of the number of baby universes with minimal neck as a function of their rescaled size x, for $\kappa_0 = 2.2$ and $\Delta = 0.4$. Distributions are normalized by the total number of baby universes in constant-time slices with $N_3 > 400$. This number grows with the total spacetime volume N_4, which is 45.5 k (bottom), 91 k (middle) and 181 k (top curve).

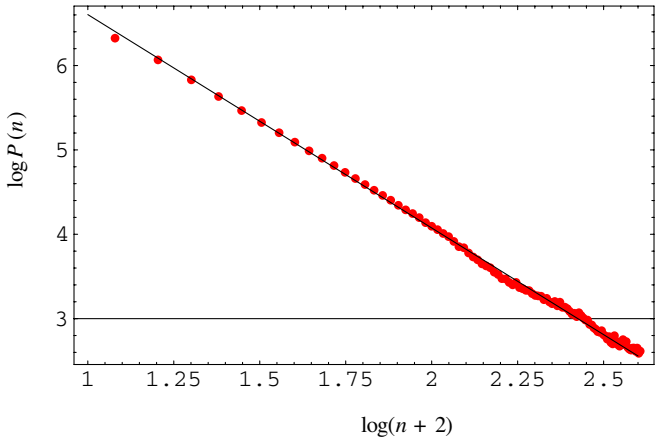

FIG. 17 (color online). Distribution $P(n)$ of the coordination numbers n of vertices in a three-dimensional spatial slice, for $\kappa_0 = 2.2$ and $\Delta = 0.4$. The straight line represents a numerical fit to formula (53), with $n_0 = 2$.

both baby and parent universes have an asymptotic distribution of the form (48).) Since it is very difficult in the present set-up to collect data for any particular fixed value of N_3, we have performed "integrated" measurements to determine $\gamma_{\rm str}$, by collecting the distribution of the number of baby universes of a given x for various volumes $N_3 > 400$. Also in this case we expect the distribution of baby universes to follow

$$P(x) \propto x^{-2+\gamma_{\rm str}}\left(1 + \frac{d}{x} + \cdots\right), \tag{52}$$

with a constant d depending now on the range of three-volumes N_3 over which we have averaged the distribution. The resulting distributions for $\kappa_0 = 2.2$, $\Delta = 0.4$ and total system sizes $N_4 = 45.5$, 91 and 181 k are shown in Fig. 16. Although the measurement is of rather poor quality, and—depending on which range of x is used for the fit—the uncertainty in $\gamma_{\rm str}$ rather big, the approximate linearity of the plots strongly suggests that the distribution is indeed dominated by a power law for x. Fitting $\gamma_{\rm str}$ to formula (52), we obtain $\gamma_{\rm str} = 0.35 \pm .09$.

Another, seemingly independent, way of characterizing the short-distance behavior of the spatial slices S is by measuring the coordination number of vertices in S, i.e. the number n_v of spatial tetrahedra sharing a given vertex v.[13] In the simulations, we observe vertices with relatively high coordination numbers n, and a distribution of n which can be approximated a simple power law

$$P(n) \propto \frac{1}{(n + n_0)^{1+\alpha}}. \tag{53}$$

[13]Note that for a 3d manifold there is a linear relation between the coordination number of a vertex v and the number of links emerging from v.

As usual, we have included a finite shift n_0 to take into account finite-size effects. For a three-dimensional triangulation, $n \geq 4$ and n may take only even values.

Figure 17 illustrates the distribution of coordination numbers for $4 \leq n \leq 200$, measured for a system with $\kappa_0 = 2.2$, $\Delta = 0.4$, $t = 40$ and system size $N_4 = 181$ k. The data points have been collected from spatial slices with three-volume $N_3 > 500$, and can be seen to behave perfectly linearly on the log-log plot. The straight line in Fig. 17 corresponds to a fit with $\alpha = 1.53$. In theories of random geometry, this type of power-law behavior of the vertex coordination number was first observed in dynamically triangulated bosonic string theory [60]. The value of the exponent α extracted from the data by χ^2-fits depends slightly on the choice of n_0 and of the cut-off in the data. Our estimate is $\alpha = 1.53 \pm 0.05$.

Another way to determine α is by studying the distribution of points with the largest coordination number as a function of the spatial volume N_3 (or the total number of vertices $N_0(N_3)$, the two numbers being proportional for the phase of four-dimensional gravity we are considering here). One expects a behavior of the form

$$P(n > n_{\rm max}(T)) \propto \frac{1}{N_3(T)}, \tag{54}$$

where $n_{\rm max}(T)$ denotes the maximal coordination number for a particular three-dimensional triangulation T. The proportionality (54) is expected to be valid if the distribution $P(n)$ is such that a typical $n_{\rm max}(T)$ is so small that it is not influenced by the fact that the volume $N_3(T)$ contains only a finite number $N_0(T)$ of vertices. (Clearly, $n_{\rm max}(T)$ cannot be larger than $N_0(T)/2$.) Under this assumption the orders n_v of the $N_0(T)$ vertices v in T are representative of the distribution $P(n)$. Since there are $N_0(T)$ of them, the chance of "drawing" an (abstract) vertex from the distribution $P(n)$ with a coordination number $n > n_{\rm max}(T)$ is of

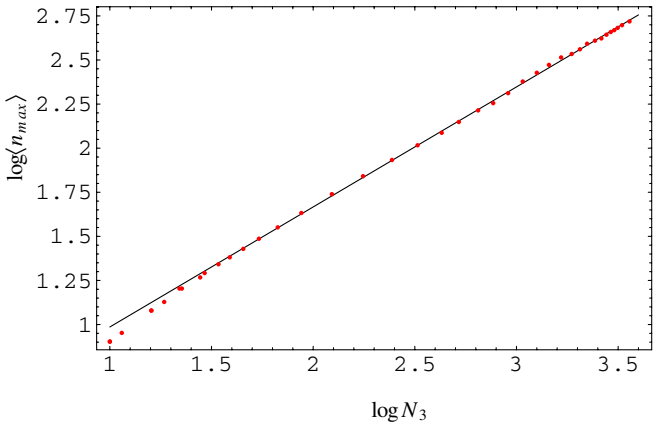

FIG. 18 (color online). Distribution of the largest coordination number $n_{\max}$ as a function of the spatial volume N_3, for $\kappa_0 = 2.2$, $\Delta = 0.4$, $t = 40$ and $N_4 = 91.1\ k$.

the order $1/N_0(T)$, which, given $N_0(N_3) \propto N_3$, is equivalent to (54). Consequently, using the scaling (53), we obtain that

$$n_{\max}(N_3) \propto N_3^{1/\alpha}. \tag{55}$$

To check this property, we measure for each spatial slice S the largest coordination numbers in S. Since these fluctuate considerably, we measure the average of the three largest values for each S. We then follow a strategy similar to that adopted for the measurement of the Hausdorff dimension. Namely, we collect data pairs $\{N_3, n_{\max}\}$, sort the resulting set by volume N_3 and average over a set of 1000 measurements. Figure 18 shows the result in the form of a log-log plot, confirming the expected linear behavior. The solid line corresponds to the value

$$\frac{1}{\alpha} = 0.681, \tag{56}$$

in fair agreement with the previous measurement from smaller correlation numbers, and the fit gives $1/\alpha = 0.681 \pm .05$, translating roughly into $\alpha = 1.468 \pm 0.12$. The origin of the uncertainty is the chosen range in the three-volume N_3 taken into account in the fitting.

D. Relation to branched polymers

The above measurements lead to the intriguing conclusion that *all* the geometric properties of the spatial slices measured so far can be modeled by a particular kind of branched polymers[14], as we will now go on to explain.

A (planar) branched polymer is an (abstract) one-dimensional polymer which admits arbitrary branching. It is modeled by (abstract) connected planar graphs which contain no loops. As a consequence, cutting any link of such a graph will result in two disconnected graphs. At each vertex an "incoming" link is allowed to "branch" into $n-1$ "outgoing" links with probability p_n. The statistical model of (rooted) branched polymers is then defined by the partition function

$$Z_{BP}(\mu) = \sum_N e^{-\mu N} Z_{BP}(N) \tag{57}$$

$$Z_{BP}(N) = \sum_{BP_N} \rho(BP_N), \qquad \rho(BP_N) = \prod_{n=1}^{N} p_n, \tag{58}$$

where the summation is over all branched polymers with N vertices, and the weight $\rho(BP)$ is the product of the branching probabilities. One can also embed the abstract branched polymers in a target space, either a lattice or R^d. In the latter case, it is convenient to work with a quadratic action $(x_u - x_v)^2$ for pairs of nearest-neighbor vertices u and v with coordinates x_u and x_v, and perform an additional integration over the target-space coordinates in the partition function.

The fractal properties of branched polymers are well understood. The leading behavior for large N is an analogue[15] of Eq. (48), namely,

$$Z_{BP}(N) \sim N^{\gamma-2} e^{\mu_0 N}, \tag{59}$$

where γ can take a range of real values, depending on the branching probability p_n. The intrinsic Hausdorff dimension $d_h^{(in)}$ of branched polymers with $\gamma > 0$ is [61–63]

$$d_h^{(in)} = \frac{1}{\gamma}, \tag{60}$$

with spectral dimension given by [41,42]

$$d_s = \frac{2}{1+\gamma}. \tag{61}$$

We note that formulas (60) and (61) already provide a close match with our data if we identify γ with the γ_{str} of the simulations. As we will see, there is indeed a concrete branched-polymer model which has the γ-value we have observed. In regularized bosonic string theory one is naturally led to studying branched polymers with branching weight [60]

$$p_n \sim \frac{1}{n^\alpha} \text{ for } n \gg 1. \tag{62}$$

Generically, the value of γ for a given α is

$$\begin{aligned} \gamma(\alpha) &= 1/2 \quad \text{for} \quad \alpha \le 1, \\ \gamma(\alpha) &= 1-\alpha \quad \text{for} \quad 1 < \alpha, \end{aligned} \tag{63}$$

which does not cover the γ-range we are interested in.

[14]In combinatorics, branched polymers are conventionally called rooted trees, where "rooted" means that one link or vertex is marked, and therefore distinguished from the rest.

[15]The difference between the power $\gamma - 2$ in Eq. (59) and $\gamma - 3$ of Eq. (48) arises because of the use of *rooted* branched polymers, which gives rise to an extra factor of N.

However, if the partition function satisfies a certain technical condition[16], the relations (63) are changed to

$$\begin{aligned} \gamma(\alpha) &= (\alpha-1)/\alpha \quad \text{for} \quad 1<\alpha<2 \\ \gamma(\alpha) &= 1/2 \qquad\quad \text{for} \quad 2\leq\alpha \end{aligned} \tag{65}$$

([63], and see [18] for a detailed discussion). While the associated condition (64) seems rather artificial from the perspective of branched polymers, it appears in a natural way if the branched polymers emerge as a limit of higher-dimensional models like noncritical strings with central charge $c>1$. As a matter of fact, the generic value of γ in this case is 1/3 [62]. Summarizing the critical exponents for this particular class of branched polymers,

$$\gamma=\frac{1}{3}, \qquad d_h^{(\mathrm{in})}=3, \qquad d_s=\frac{3}{2}, \qquad \alpha=\frac{3}{2}, \tag{66}$$

we see that within the measuring accuracy, *they are precisely the numbers characterizing the spatial geometries of causal dynamical triangulations at constant time*. Although the vertex order n_v of our three-dimensional triangulations has *a priori* nothing to do with the branching of polymers, the above results are a strong hint that there effectively is such a connection. While this confirms our earlier assertion that the geometry of the spatial slices behaves very nonclassically, it opens the exciting possibility that quantum gravity as described by this model may be amenable to analytic approximations, precisely as was the case in the study of noncritical strings with $c>1$ [62].

VII. NONCLASSICAL STRUCTURE OF THE UNIVERSE: THE GEOMETRY OF "THICK" SPATIAL SLICES

Another substructure of spacetime whose geometry can be investigated straightforwardly are what we shall call thick spatial slices, namely, the sandwiches of geometry contained in between two adjacent spatial slices of integer times τ and $\tau+1$, with topology $I\times S^3$. As illustrated in Fig. 1, they are made up of four-simplices of types (4,1) and (3,2) and their time-reversed counterparts (1,4) and (2,3). Because of their finite time extension, one might expect the geometry of the thick slices to behave more "classically", and this is indeed corroborated by our simulations, which include a measurement of the Hausdorff and spectral dimension of the thick slices.

A convenient way to represent a sandwich geometry is by considering the three-dimensional piecewise flat geometry that results by cutting the thick slice at time $\tau+1/2$. The analogous procedure in one dimension less, which is easier to visualize, gives a generalized two-dimensional triangulation consisting of triangles and squares [33,34,54]. The triangles are the intersection surfaces of (3,1)- and (1,3)-tetrahedra, and the squares those of (2,2)-tetrahedra. In one dimension higher, the fundamental building blocks are no longer tetrahedra but four-simplices. Consequently, the intersection patterns are three-dimensional flat building blocks, namely, spatial tetrahedra from slicing the (4,1)- and (1,4)-simplices, and spatial triangular prisms from slicing the (3,2)- and (2,3)-simplices. In order to distinguish between a tetrahedron that comes from cutting a (4,1)-simplex from one associated with an upside-down, (1,4)-simplex, one color-codes the links of the intersection hypersurface into red and blue, say. The red links are those that will be "shrunk away" when the constant-time surface approaches the integer-time $\tau+1$, and similarly the blue links will disappear as the hypersurface is moved towards time τ. As a result, the tetrahedra have all links of one color, whereas the prisms are always bi-coloured (see also [22]). Note that the average spatial volume in terms of counting three-dimensional building blocks is larger (by a factor of about 2.5) at slices of half-integer time, because—unlike at integer times—all four-simplices between τ and $\tau+1$ contribute to the counting.

A. The Hausdorff dimension

To determine the Hausdorff dimension d_H of the thick slices, we pick a random four-simplex from such a slice, or, equivalently, a random three-dimensional building block from the corresponding intersection pattern at half-integer time. Continuing in this three-dimensional representation of the slice geometry, we proceed exactly as we did when measuring the Hausdorff dimension d_h of the spatial slices at integer-τ. Starting from the randomly chosen initial three-dimensional building block, we move out, one step at a time, to the nearest neighbors at distance r, from the previous set of building blocks at distance $r-1$. In terms of four-simplices, this means we never move out to simplices earlier than τ or later than $\tau+1$, that is, by definition we never leave the thick slice. At each step, we keep track of the number $n(r)$ of building blocks, whose sum is equal to the total slice volume N,

$$\sum_{r=0}^{r_{\max}} n(r)=N, \tag{67}$$

and which enables us to compute the average linear size

$$\langle r\rangle=\frac{1}{N}\sum_r rn(r) \tag{68}$$

[16]For (65) to hold one needs

$$\frac{dZ_{BP}(\mu)}{d\mu}<0 \quad \text{for} \quad \mu>\mu_0, \qquad \left.\frac{dZ_{BP}(\mu)}{d\mu}\right|_{\mu=\mu_0}=\infty, \tag{64}$$

which is naturally satisfied for some branched-polymer models coming from noncritical string theory [62].

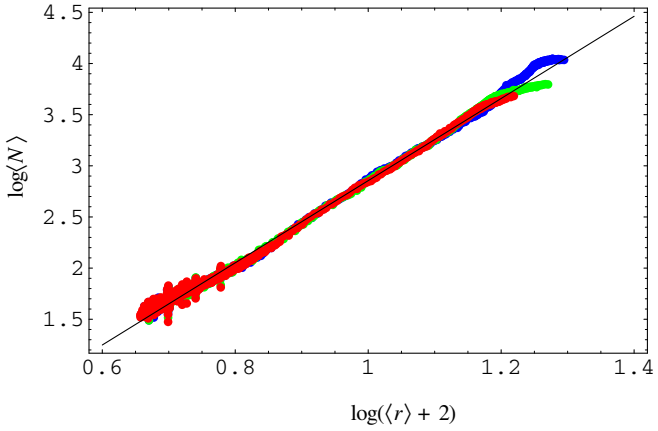

FIG. 19 (color online). Log-log plot of the average linear geodesic size $\langle r\rangle_N$ versus the volume N of a thick slice. The straight line corresponds to a Hausdorff dimension $d_H = 4$.

of the thick slice. For a given slice of volume N, this process is then repeated $N_4/100 + 1$ times with randomly chosen initial building blocks. The average size $\langle r\rangle$ is again averaged over this set and the data pair $\{\langle\langle r\rangle\rangle, N\}$ stored. Using the same procedure as described following formula (43) above, we extract the Hausdorff dimension d_H from the relation

$$N_4 \propto (\langle r\rangle + r_0)^{d_H}, \tag{69}$$

with a finite constant r_0 taking into account finite-size corrections. The results are presented in Fig. 19 in the form of a log-log plot. The straight line corresponds to $d_H = 4$, and the best fitted value is $d_H = 4.01 \pm 0.05$. Measurements were performed on spacetimes with total size $\tilde{N}_4 = 20, 40$ and 80 k, at $\kappa_0 = 2.2$, $\Delta = 0.6$ and $t = 80$. We conclude that the transition from a genuine constant-time slice to a thick slice adds one extra dimension to the Hausdorff dimension – the thickened slice already "feels" some aspects of the four-dimensionality of the full spacetime. Note that this would not be true for a thick slice of a classical, regular lattice, whose Hausdorff dimension would be the same as that of a thin slice. The likely mechanism for the dimensional increase in the triangulations is the appearance of "short-cuts" between two tetrahedral building blocks, say, once one moves slightly away from a slice of integer-τ.

B. The spectral dimension

Next, we turn to the spectral dimension d_S of the thick slices. When adapting our earlier measurement of the spectral dimension d_s of spatial slices, we have to take into account that the tetrahedral building blocks in the three-dimensional intersection pattern at half-integer τ have four neighbors, whereas the prisms have five. We start from an initial probability distribution

$$K_T(i, i_0, \sigma = 0) = \delta_{i,i_0} \tag{70}$$

concentrated at a randomly chosen three-dimensional building block with label i_0 in the three-dimensional "triangulation" T (consisting of tetrahedra and triangular prisms), and define the evolution process by

$$K_T(j, i_0; \sigma + 1) = \sum_{k\rightarrow j} \frac{1}{g_k} K_T(k, i_0; \sigma), \tag{71}$$

where g_i denotes the number of neighbors of building block i, and $k \rightarrow j$ are the nearest neighbors of the "simplex" j (which can now also be a prism). By construction, the total probability

$$\sum_i K_T(i, i_0; \sigma) = 1 \tag{72}$$

is conserved. As before, we measure the return probability $K_T(i_0, i_0; \sigma)$. After the appropriate averaging over initial points i_0 and triangulations T we obtain the quantum return probability $P_N(\sigma)$ as a function of the number of building blocks N in the triangulations T (we keep the number N approximately constant in the triangulations included in the average). The expected behavior

$$P_N(\sigma) \propto \sigma^{-d_S/2} + \text{finite-size corrections} \tag{73}$$

defines a spectral dimension d_S, which in general will be different from the spectral dimension d_s determined for the constant-time slices. The value of d_S is extracted by mea-

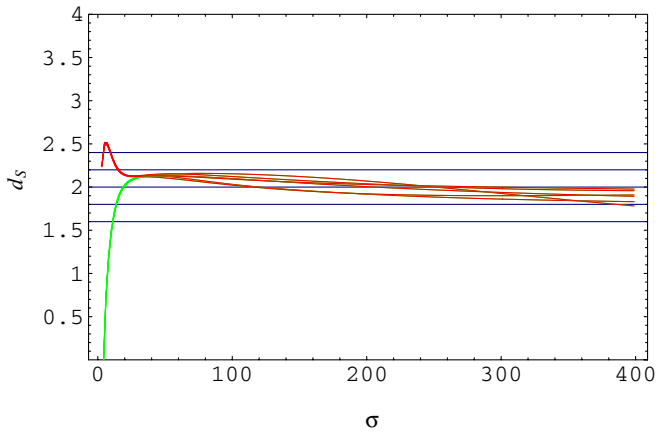

FIG. 20 (color online). The logarithmic derivative of the return probability for $\kappa_0 = 2.2$ and $\Delta = 0.6$ and thick slices of volumes N between 900 and 2000. The measurement was performed for a system with $N_4 = 161\ k$ and $t = 80$. Curves extrapolating between even evolution times decrease rapidly at small σ, whereas curves of odd times stay above $d_S = 2$ at small times.

suring the logarithmic derivative of $P_N(\sigma)$ as a function of the evolution time σ,

$$d_S(\sigma) = -2\frac{d\log P_N(\sigma)}{d\log\sigma}. \tag{74}$$

The results of our measurements are displayed separately for even and odd times in Fig. 20, since the behavior of $P_N(\sigma)$ is different for very small σ (as already observed in our previous measurements of spectral dimensions). As seen in the figure, beyond small σ we do not find the perfect constant logarithmic derivative observed earlier for the thin slices at integer time. If we nevertheless treat the output curves as constants and take their mean value as representative of the logarithmic derivative d_S (assuming it *is* σ-independent), we obtain $d_S = 2.0 \pm 0.2$. Although it lies above the value d_s for the spectral dimension of the spatial slices, this dimensionality is still highly nonclassical, and reflects the presence of some intermediate regime between a purely spatial and a purely spacetime geometry.

C. Baby universes

To further characterize the geometry of thick slices, we also looked into its baby universe structure. Minimal necks can take the form of either four triangles, forming the surface of a tetrahedron, or of two triangles and three squares, forming the surface of a triangular prism (of course, *without* an interior tetrahedron or prism being located there). It turns out that the four-dimensional manifold constraints, which ensure that the four-simplices are glued in a way that results in a simplicial *manifold*, impose severe restrictions on the types of baby universes with minimal necks that can occur.[17] For a tetrahedral minimal neck, the baby universe which branches off there can only contain building blocks which are tetrahedra of the same color. Minimal necks of the form of a prism cannot occur altogether. We attempted to measure the distribution of ''monochrome'' tetrahedral baby universes, but found them to be small in size, within a range practically independent of the slice volume N. We did not check for baby universes with larger necks. Our tentative conclusion is that the microscopic structure of the thick slices is more regular than that of the genuine spatial slices of fixed constant time.

It is tempting to conjecture that the absence of baby universes means that the entropy function $\mathcal{N}(V)$ for the thick spatial slices has the functional form (49) rather than (48), which was the form observed for the thin spatial slices at fixed integer time. As mentioned in Sec. VI C, the entropy behavior (49) signals an almost complete suppression of baby universes. Moreoever, if the exponent ν in Eq. (49) was equal to 1/3, it would fit neatly with the observation that the effective macroscopic action (40), which reproduces so well the macroscopic four-dimensional features we observe in the simulations, *does* contain the characteristic linear term in the scale factor $a(\tau)$ (corresponding to a factor $V_3^{1/3}(\tau)$ in terms of the continuum three-volume). It would also be in line with our expectation that the structure of the thick spatial slices, rather than that of the thin slices at fixed time should relate most directly to the global four-dimensional structure.

VIII. SUMMARY AND OUTLOOK

This paper describes the currently known geometric properties of the quantum universe generated by the method of causal dynamical triangulations, as well as the general phase structure of the underlying statistical model of four-dimensional random geometries. The main results are as follows. An extended quantum universe exists in one of the three observed phases of the model, which occurs for sufficiently large values of the bare Newton's constant G and of the asymmetry Δ, which quantifies the finite relative length scale between the time and spatial directions. In the two other observed phases, the universe disintegrates into a rapid succession of spatial slices of vanishing and nonvanishing spatial volume (small G), or collapses in the time direction to a universe that only exists for an infinitesimal moment in time (large G, vanishing or small Δ). In either of these two cases, no macroscopically extended spacetime geometry is obtained.

By measuring the (Euclidean) geometry of the dynamically generated quantum spacetime[18] in the remaining phase, in which the universe appears to be extended in space and time, we collected strong evidence that it behaves as a *four*-dimensional quantity on large scales. First, finite-size scaling of the volume-volume correlator for spatial slices is observed when the time variable is rescaled by the fourth root of the discrete four-volume, Eq. (11), within measuring accuracy. Second, the large-scale spectral dimension of the universe, determined from a diffusion process on the quantum ensemble of geometries, is compatible with the value 4.

The dynamical derivation of the correct classical result for the dimension from a completely nonperturbative path-integral setting provides a considerable boost to our efforts to construct a theory of quantum gravity by the method of causal dynamical triangulations. Furthermore, we were able to show that the universe possesses other features of classical geometry at sufficiently large scales. Namely, using the four-dimensionality at large scales, we derived an effective Euclidean action for the scale factor of the universe (equivalently, the volume of its spatial slices). For

[17] Analogous manifold conditions for intersection graphs in three-dimensional simplicial spacetimes were formulated in [34].

[18] Since our universe is a weighted quantum superposition of geometries, all ''measurements'' refer to expectation values of geometric operators in the quantum ground state.

the case of fixed spacetime volume, this action coincides *up to an overall sign* with a simple minisuperspace action frequently used in quantum cosmology. Again, we believe that this is a highly nontrivial and very exciting result. It has already enabled us to derive a ''wave function of the universe'' from first principles [20]. The change in sign of the action implies that the Euclidean sector of our quantum gravity model is well-defined. This is a welcome result since, unlike in standard quantum cosmology, no *ad hoc* cure is needed to deal with a conformal kinetic term that renders the action unbounded below. Some care is required in interpreting it, since we still need to perform an inverse Wick rotation to get back to the physical, Lorentzian sector of the theory. A detailed discussion will appear elsewhere.

Returning to the analysis of the quantum geometry of our universe, we gained further insights by performing measurements of a more local nature by looking at the intrinsic geometry of thin and thick spatial slices. A thin slice is by definition a spatial geometry at fixed integer time somewhere inside a universe, and a thick slice a piece of spacetime contained between two adjacent thin slices. We found that in general the measured observables exhibit nonclassical behavior, in the sense that dynamically determined dimensionalities of the slices do not coincide with the values one would have expected naively for the corresponding submanifolds of a *classical* four-dimensional spacetime. This result is not in contradiction with the four-dimensional behavior of the universe at large scales, but underscores the fact that the local geometry of the quantum spacetime has highly nonclassical features.[19]

We found that the measured Hausdorff dimension of thin slices comes out as 3 with good accuracy, but that the spectral dimension is only around 1.5! By making additional measurements of the distributions of vertex coordination numbers and of baby universes in the thin slices we were able to show that the entire set of parameters is matched by the critical exponents of a particular class of branched polymers, potentially opening a new window to an analytic investigation of quantum spacetime.

The thick slices were found to have Hausdorff dimension 4 within measuring accuracy, and a spectral dimension of around 2. This, and the apparent absence of baby universes of appreciable size indicate that the geometry of the thick slices represents a genuinely intermediate case between that of the thin slices and of the full spacetime. In particular, their geometry—although far from being classical—seems to be more regular than that of the thin slices.

The most local measurement of quantum geometry so far is that of the spectral dimension of spacetime *at short distances*, which provides another quantitative measure of the nonclassicality of geometry. As we have seen, the spectral dimension changes smoothly from about 4 on large scales to about 2 on small scales. Not only does this (to our knowledge) constitute the first dynamical derivation of a scale-dependent dimension in full quantum gravity, but it may also provide a natural short-distance cut-off by which the nonperturbative formulation evades the ultraviolet infinities of perturbative quantum gravity. Remarkably, evidence for a dimensional reduction from four to two has been found recently in the so-called exact renormalization group approach to (Euclidean) quantum gravity, truncated to a finite-dimensional parameter space [2]. One could be particularly encouraged by the fact that despite very different starting points and quantization methods the two approaches nevertheless seem to lead to compatible results.

In summary, what emerges from our formulation of nonperturbative quantum gravity as a continuum limit of causal dynamical triangulations is a compelling and rather concrete geometric picture of *quantum spacetime*. Quantum spacetime possesses a number of large-scale properties expected of a four-dimensional classical universe, but at the same time exhibits a nonclassical and nonsmooth behavior microscopically, due to large quantum fluctuations of the geometry at small scales. These fluctuations ''conspire'' to create a quantum geometry that is effectively two-dimensional at short distances.

Of course, our large-scale measurements of geometry so far do not characterize the classical properties of our quantum spacetime completely, and further work is under way to determine its large-scale curvature properties, and check that Newton's inverse square law can be recovered in an appropriate limit (see [64] for related previous attempts). Having established the existence of a meaningful classical limit opens the door to the ultimate subject of our interest, the quantum behavior of the local gravitational degrees of freedom. On the one hand, together with appropriate matter degrees of freedom, they should be able to describe the quantum behavior of the very early universe, which may have left an imprint on the cosmic microwave background radiation we observe today. On the other hand, they will characterize the fluctuations around a large-scale classical background, like that of our present universe, leading to quantifiable deviations from the predictions of classical relativity.

[19]One should keep in mind that slices of constant time are in no way physically distinguished in a theory of pure gravity, and their geometric properties therefore not directly related to physical observables.

[1] M. Reuter Phys. Rev. D **57**, 971 (1998).
[2] O. Lauscher and M. Reuter, Phys. Rev. D **65**, 025013 (2002); hep-th/0205062.
[3] W. Souma, Prog. Theor. Phys. **102**, 181 (1999); M. Reuter and F. Saueressig, Phys. Rev. D **66**, 125001 (2002); Phys. Rev. D **65**, 065016 (2002); D. F. Litim, Phys. Rev. Lett. **92**, 201301 (2004); M. Reuter and H. Weyer, J. Cosmol. Astropart. Phys. 12 (2004) 001; A. Bonanno and M. Reuter, J. High Energy Phys. 02 (2005) 035.
[4] T. Thiemann, Lect. Notes Phys. **631**, 41 (2003).
[5] C. Rovelli, *Quantum Gravity* (Cambridge University Press, Cambridge, United Kingdom, 2004).
[6] H. Nicolai, K. Peeters, and M. Zamaklar, hep-th/0501114.
[7] A. Perez, Class. Quant. Grav. **20**, R43-R104 (2003).
[8] J. Ambjørn and R. Loll Nucl. Phys. **B536**, 407 (1998).
[9] J. Ambjørn, J. Jurkiewicz, and R. Loll, Phys. Rev. Lett. **85**, 924 (2000).
[10] J. Ambjørn, J. Jurkiewicz, and R. Loll, Nucl. Phys. **B610**, 347 (2001).
[11] J. Ambjørn and J. Jurkiewicz, Phys. Lett. B **278**, 42 (1992).
[12] J. Ambjørn and J. Jurkiewicz Nucl. Phys. **B451**, 643 (1995).
[13] P. Bialas, Z. Burda, A. Krzywicki, and B. Petersson, Nucl. Phys. **B472**, 293 (1996).
[14] P. Bialas, Z. Burda, B. Petersson, and J. Tabaczek, Nucl. Phys. **B495**, 463 (1997).
[15] S. Catterall, J. B. Kogut, and R. Renken Phys. Lett. B **328**, 277 (1994).
[16] S. Catterall, R. Renken, and J. B. Kogut Phys. Lett. B **416**, 274 (1998).
[17] B. V. de Bakker and J. Smit, Nucl. Phys. **B439**, 239 (1995).
[18] J. Ambjørn, B. Durhuus, and T. Jonsson, *Quantum Geometry* (Cambridge University Press, Cambridge, England, 1997).
[19] J. Ambjørn, J. Jurkiewicz, and R. Loll, Phys. Rev. Lett. **93**, 131301 (2004).
[20] J. Ambjørn, J. Jurkiewicz, and R. Loll, Phys. Lett. B **607**, 205 (2005).
[21] J. Ambjørn, J. Jurkiewicz, and R. Loll, hep-th/0505113.
[22] B. Dittrich and R. Loll, gr-qc/0506035.
[23] J. W. Alexander, Ann. Math. **31**, 292 (1930).
[24] U. Pachner, Arch. Math. **30**, 89 (1978).
[25] M. Gross and S. Varsted, Nucl. Phys. **B378**, 367 (1992).
[26] J. Ambjørn and S. Varsted, Nucl. Phys. **B373**, 557 (1992).
[27] J. Ambjørn, D. V. Boulatov, A. Krzywicki, and S. Varsted, Phys. Lett. B **276**, 432 (1992).
[28] J. Ambjørn, B. Durhuus, and T. Jonsson, J. Phys. A **21**, 981 (1988).
[29] S. Weinberg, in *General relativity: Einstein centenary survey*, edited by S. W. Hawking and W. Israel (Cambridge University Press, Cambridge, England, 1979) p. 790.
[30] H. Kawai, Y. Kitazawa, and M. Ninomiya, Nucl. Phys. **B467**, 313 (1996); Nucl. Phys. **B404**, 684 (1993); Nucl. Phys. **B393**, 280 (1993); H. Kawai and M. Ninomiya Nucl. Phys. **B336**, 115 (1990).
[31] H. W. Hamber, Phys. Rev. D **61**, 124008 (2000).Nucl. Phys. **B400**, 347 (1993).
[32] M. E. Agishtein and A. A. Migdal Nucl. Phys. **B385**, 395 (1992).
[33] J. Ambjørn, J. Jurkiewicz, and R. Loll, Phys. Lett. B **581**, 255 (2004).
[34] J. Ambjørn, J. Jurkiewicz, R. Loll, and G. Vernizzi, J. High Energy Phys. 09 (2001) 022.
[35] S. Catterall, G. Thorleifsson, J. B. Kogut, and R. Renken Nucl. Phys. **B468**, 263 (1996).
[36] M. E. J. Newman and G. T. Barkema, *Monte Carlo Methods in Statistical Physics* (Oxford University Press, Oxford, England, 1999).
[37] H. Kawai, N. Kawamoto, T. Mogami, and Y. Watabiki Phys. Lett. B **306**, 19 (1993).
[38] J. Ambjørn and Y. Watabiki Nucl. Phys. **B445**, 129 (1995).
[39] S. Catterall, G. Thorleifsson, M. J. Bowick, and V. John Phys. Lett. B **354**, 58 (1995).
[40] J. Ambjørn, J. Jurkiewicz, and Y. Watabiki, Nucl. Phys. **B454**, 313 (1995).
[41] T. Jonsson and J. F. Wheater, Nucl. Phys. **B515**, 549 (1998).
[42] J. Ambjørn, D. Boulatov, J. L. Nielsen, J. Rolf, and Y. Watabiki, J. High Energy Phys. 02 (1998) 010.
[43] J. Ambjørn, K. N. Anagnostopoulos, T. Ichihara, L. Jensen, and Y. Watabiki, J. High Energy Phys. 11 (**1998**) 022.
[44] J. Ambjørn and K. N. Anagnostopoulos, Nucl. Phys. **B497**, 445 (1997).
[45] J. B. Hartle and S. W. Hawking, Phys. Rev. D **28**, 2960 (1983).
[46] G. W. Gibbons and S. W. Hawking, *Euclidean Quantum Gravity* (World Scientific, Singapore, 1993).
[47] A. Vilenkin, Phys. Lett. B **117**, 25 (1982); Phys. Rev. D **30**, 509 (1984).
[48] A. D. Linde, Lett. Nuovo Cimento **39**, 401 (1984).
[49] V. A. Rubakov, Phys. Lett. B **148**, 280 (1984).
[50] J. J. Halliwell and J. Louko, Phys. Rev. D **39**, 2206 (1989).
[51] J. J. Halliwell and J. B. Hartle, , Phys. Rev. D **41**, 1815 (1990).
[52] A. Vilenkin, Phys. Rev. D **50**, 2581 (1994).
[53] A. Vilenkin, in *The future of theoretical physics and cosmology*, edited by G. W. Gibbons, E. P. S. Shellard, and S. J. Rankin (Cambridge University Press, Cambridge, England, 2003) p. 649.
[54] J. Ambjørn, J. Jurkiewicz, and R. Loll, Phys. Rev. D **64**, 044011 (2001).
[55] J. Ambjørn, A. Dasgupta, J. Jurkiewicz, and R. Loll, Nucl. Phys. B Proc. Suppl. **106**, 977 (2002).
[56] A. Dasgupta and R. Loll, Nucl. Phys. **B606**, 357 (2001).
[57] S. Jain and S. D. Mathur, Phys. Lett. B **286**, 239 (1992).
[58] J. Ambjørn, S. Jain, and G. Thorleifsson, Phys. Lett. B **307**, 34 (1993).
[59] J. Ambjørn, S. Jain, J. Jurkiewicz, and C. F. Kristjansen Phys. Lett. B **305**, 208 (1993).J. Ambjørn, P. Bialas, J. Jurkiewicz, Z. Burda, and B. Petersson, Phys. Lett. B **325**, 337 (1994.
[60] J. Ambjørn, B. Durhuus, and J. Fröhlich Nucl. Phys. **B275**, 161 (1986); Nucl. Phys. **B257**, 433 (1985); J. Ambjørn, B. Durhuus, J. Fröhlich, and P. Orland, Nucl. Phys. **B270**, 457 (1986).

[61] J. Ambjørn, B. Durhuus, and T. Jonsson, Phys. Lett. B **244**, 403 (1990).

[62] J. Ambjørn, B. Durhuus, and T. Jonsson, Mod. Phys. Lett. A **9**, 1221 (1994); J. Ambjørn, B. Durhuus, T. Jonsson, and G. Thorleifsson, Nucl. Phys. **B398**, 568 (1993).

[63] J. Jurkiewicz and A. Krzywicki Phys. Lett. B **392**, 291 (1997).

[64] H. W. Hamber and R. M. Williams, Nucl. Phys. **B435**, 361 (1995).B. V. de Bakker and J. Smit, Nucl. Phys. **B484**, 476 (1997).

[65] J. Ambjørn, K. Anagnostopoulos, T. Ichihara, L. Jensen, N. Kawamoto, Y. Watabiki, and K. Yotsuji, Nucl. Phys. **B511**, 673 (1998).